



ATLAS CONF Note

ATLAS-CONF-2025-008

6th July 2025



Observation of a cross-section enhancement near the $t\bar{t}$ production threshold in $\sqrt{s} = 13$ TeV $p p$ collisions with the ATLAS detector

The ATLAS Collaboration

A measurement is presented of $t\bar{t}$ production in the invariant-mass region near the pair production threshold, $m_{t\bar{t}} \sim 345$ GeV, in final states with two charged leptons and multiple jets. The measurement is based on 140 fb^{-1} of proton–proton collision data collected at $\sqrt{s} = 13$ TeV with the ATLAS detector. The data are compared to two models of $t\bar{t}$ production: a baseline model including only perturbative QCD (pQCD) predictions for the hard process, and an extended model that, in addition to the pQCD predictions, incorporates state-of-the-art Monte Carlo simulations of colour-singlet quasi-bound-state formation near the $t\bar{t}$ threshold. The agreement between the data and the models is quantified via a profile-likelihood fit to the reconstructed $m_{t\bar{t}}$ distributions, in bins of two angular observables sensitive to spin-correlations in the $t\bar{t}$ system. An excess of events is observed over the baseline pQCD prediction, with an observed significance of 7.7 standard deviations. This excess is consistent with the formation of colour-singlet, S -wave, quasi-bound $t\bar{t}$ states as predicted by non-relativistic QCD, and corresponds to an observed cross-section of $9.0 \pm 1.3\text{ pb}$.

1 Introduction

The unprecedented centre-of-mass energies and luminosities of proton–proton collisions delivered by the Large Hadron Collider (LHC) at CERN enable the study of the top quark, the heaviest known elementary particle, across a broad kinematic range. The high top-quark production rate at the LHC and the excellent event reconstruction capabilities of the ATLAS detector allow for precision beyond expectations in complex final states. This includes precision measurements and direct searches for new phenomena in distinct parts of the phase space, including previously inaccessible ones characterised by high Lorentz boosts of the top quarks.

In recent years, growing attention has turned to the opposite end of the kinematic spectrum where top quarks are produced with low velocities in their centre-of-mass frame. In the case of top-quark pair ($t\bar{t}$) production, the dominant production mode for top quarks at the LHC, this regime corresponds to events in which the invariant mass of the system, $m_{t\bar{t}}$, is close to the production threshold, $m_{t\bar{t}} \approx 2m_t \approx 345$ GeV. In this kinematic regime, a large fraction of the $t\bar{t}$ events are produced in a colour-singlet state and are maximally entangled [1, 2]. It was by focusing exclusively on events with $m_{t\bar{t}}$ near the production threshold that the first observation of quantum entanglement at the LHC became possible [3, 4]. Moreover, the $t\bar{t}$ production cross-section in the threshold region is sensitive to the top Yukawa coupling, which can be constrained indirectly via measurements targeting this regime [5].

An intriguing property of these non-relativistic $t\bar{t}$ systems close to the production threshold is the formation of colour-singlet, S-wave, quasi-bound-states with masses just below the production threshold, which are referred to as “toponia”, in analogy to the bound states of the lighter b - and c -quarks. Unlike the latter, the large top-quark mass and its correspondingly short lifetime prevent the formation of conventional Breit-Wigner resonances that decay via annihilation of their constituent quarks. Instead, these quasi-bound-states decay via the weak decay of the individual top or antitop quark [6] and are not expected to appear as sharp resonance peaks in the $m_{t\bar{t}}$ spectrum. Instead, they appear as a local enhancement that is broader than the hadronic resonances formed of the lighter quarks but has a width well below the current experimental resolution. First hypothesised in the late 1980s [7–9], well before the 1995 discovery of the top quark [10, 11], measurements of $t\bar{t}$ quasi-bound states would provide a stringent probe of quantum chromodynamics (QCD) in the non-relativistic regime (NRQCD) [12, 13].

A key challenge of measurements and searches targeting the $t\bar{t}$ production threshold lies in the accurate modelling of NRQCD effects, as well as missing higher-order contributions in perturbative QCD (pQCD), and off-shell effects in the top-quark decay. Calculations of the $t\bar{t}$ invariant mass spectrum that incorporate NRQCD effects have been developed in the past [14, 15], and now also include the resummation of soft and collinear gluon emissions near the threshold [1, 16]. They predict an enhancement of $t\bar{t}$ production below the $t\bar{t}$ threshold compared to next-to-leading order (NLO) and next-to-next-to-leading order (NNLO) pQCD predictions due to the formation of quasi-bound-states. The resummation of additional terms that scale in powers of α_s/v [17, 18] (where v is the velocity of the top quarks) also yields an enhancement of $t\bar{t}$ production below the $t\bar{t}$ threshold compared to current (N)NLO pQCD predictions. Additionally, off-shell effects and interference between $t\bar{t}$ and the production of a single top quark with a W boson (tW) at NLO in pQCD are known to be sizeable close to threshold [17], especially with regard to $t\bar{t}$ spin correlations. Predictions for a consistent NLO description of $t\bar{t}$ and tW production and decay, including quantum interference effects, have been derived for both dileptonic [19] and semileptonic [20] final states.

Tensions between data and current Monte Carlo (MC) models for $t\bar{t}$ production have been observed in several precision measurements near the kinematic threshold by both the ATLAS [3, 21, 22] and CMS [4,

[23, 24] collaborations. The MC models used in these measurements do not include NRQCD effects. They provide matrix elements (ME) at NLO accuracy in pQCD matched to a parton shower (PS) model. In some cases, the NLO predictions have additionally been reweighted to more accurate predictions at NNLO in pQCD and NLO accuracy in the electroweak coupling. The CMS collaboration has shown for two of these results [4, 24] that the observed tension between the data and these models close to the production threshold can be alleviated by supplementing pQCD predictions via a simplified model [25, 26] in which $t\bar{t}$ quasi-bound-state effects are modelled as a narrow pseudo-scalar resonance, $\eta_{t\bar{t}}$, with mass close to $2 \cdot m_t$ and no interference with pQCD $t\bar{t}$ production. Most recently, CMS reported an excess with a significance greater than five standard deviations near the $t\bar{t}$ threshold compared to the pQCD predictions, consistent with the production of a quasi-bound-state $\eta_{t\bar{t}}$ [27].

In parallel, significant progress has been made in providing a more complete MC model of contributions from NRQCD at the $t\bar{t}$ threshold, particularly concerning the inclusion of quasi-bound-states [25, 28]. In this approach, quasi-bound-state formation is described using a reweighting of the $t\bar{t}$ production MEs through the non-relativistic QCD Green's function, which includes the resummation of terms proportional to the first power in α_s/v . The associated predictions for $t\bar{t}$ quasi-bound states, referred to as $t\bar{t}_{\text{NRQCD}}$ in the following, have been shown to differ from those of the simplified pseudo-scalar model $\eta_{t\bar{t}}$ [29]. Combining these predictions with standard pQCD $t\bar{t}$ MC provides a more complete prediction of the $t\bar{t}$ threshold dynamics.

In this paper, a measurement of $t\bar{t}$ near the kinematic threshold is presented, with a particular focus on the effects of $t\bar{t}$ quasi-bound-state formation. The analysis targets dileptonic $t\bar{t}$ decays and is based on proton–proton (pp) collision data recorded with the ATLAS detector at a centre-of-mass energy of $\sqrt{s} = 13$ TeV during LHC Run 2 (2015–2018), corresponding to an integrated luminosity of 140 fb^{-1} . The measurement relies on $m_{t\bar{t}}$ and two angular observables, evaluated in the $t\bar{t}$ centre-of-mass frame, that are sensitive to $t\bar{t}$ spin-correlations. These observables were found to be powerful in selecting events with a spin-singlet contribution, which is the dominant contribution of the quasi-bound-state. A profile-likelihood fit is used to compare the level of agreement with data to two models of $t\bar{t}$ production: a baseline model including only PS-matched pQCD predictions reweighted to NNLO-QCD+NLO-EW accuracy; and an extended model that includes, in addition to the pQCD predictions, state-of-the-art MC simulations of the formation of colour-singlet quasi-bound states near the $t\bar{t}$ production threshold [25, 28]. The normalisation of the quasi-bound-state component in the extended model is a free-floating parameter in the fit and allows for a smooth extrapolation between the baseline and extended models. Its fitted value is used to extract the total observed cross-section for the quasi-bound-state contribution.

2 ATLAS detector

The ATLAS experiment [30] at the LHC is a multipurpose particle detector with a forward–backward symmetric cylindrical geometry and a near 4π coverage in solid angle.¹ It consists of an inner tracking detector surrounded by a thin superconducting solenoid providing a 2 T axial magnetic field, electromagnetic and hadronic calorimeters, and a muon spectrometer. The inner tracking detector covers the pseudorapidity

¹ ATLAS uses a right-handed coordinate system with its origin at the nominal interaction point (IP) in the centre of the detector and the z -axis along the beam pipe. The x -axis points from the IP to the centre of the LHC ring, and the y -axis points upwards. Cylindrical coordinates (r, ϕ) are used in the transverse plane, ϕ being the azimuthal angle around the z -axis. The pseudorapidity is defined in terms of the polar angle θ as $\eta = -\ln \tan(\theta/2)$. Angular distance is measured in units of $\Delta R \equiv \sqrt{(\Delta\eta)^2 + (\Delta\phi)^2}$.

range $|\eta| < 2.5$. It consists of silicon pixel, silicon microstrip, and transition radiation tracking detectors. Lead/liquid-argon (LAr) sampling calorimeters provide electromagnetic (EM) energy measurements with high granularity within the region $|\eta| < 3.2$. A steel/scintillator-tile hadronic calorimeter covers the central pseudorapidity range ($|\eta| < 1.7$). The endcap and forward regions are instrumented with LAr calorimeters for EM and hadronic energy measurements up to $|\eta| = 4.9$. The muon spectrometer surrounds the calorimeters and is based on three large superconducting air-core toroidal magnets with eight coils each. The field integral of the toroids ranges between 2.0 and 6.0 T m across most of the detector. The muon spectrometer includes a system of precision tracking chambers up to $|\eta| = 2.7$ and fast detectors for triggering up to $|\eta| = 2.4$. The luminosity is measured mainly by the LUCID–2 [31] detector which is located close to the beampipe. A two-level trigger system was used to select events [32]. The first-level trigger is implemented in hardware and used a subset of the detector information to accept events at a rate close to 100 kHz. This is followed by a software-based trigger that reduced the accepted rate of complete events to 1.25 kHz on average depending on the data-taking conditions. A software suite [33] is used in data simulation, in the reconstruction and analysis of real and simulated data, in detector operations, and in the trigger and data acquisition systems of the experiment.

3 Data and simulated event samples

The data used in this measurement were collected with the ATLAS detector in pp collisions at $\sqrt{s} = 13$ TeV during the years 2015 to 2018, corresponding to an integrated luminosity of 140 fb^{-1} [34]. Candidate events were selected online using trigger algorithms requiring at least one muon [35] or one electron [36] above a certain transverse momentum (p_T) threshold. The triggers with the lowest p_T threshold in data require $p_T > 24$ GeV and include a lepton isolation requirement. The trigger efficiency is mostly constant for leptons with $p_T > 28$ GeV. Simulated event samples are used to model the different processes expected to contribute in the regions defined in the analysis.

For all MC samples, the ATLAS simulation infrastructure [37] was used. All nominal samples as well as several alternative samples used to assess systematic uncertainties were produced with a detailed GEANT4 [38] detector simulation, while a faster simulation [39] was used for the remaining alternative background samples. Pile-up effects are modelled by overlaying minimum-bias events simulated using the soft QCD processes of PYTHIA8.1 [40] with the NNPDF2.3LO set of parton distribution functions (PDFs) [41] and the A3 [42] tune. The events are reweighted to match the pile-up conditions of each dataset corresponding to the years 2015–2018. The same offline reconstruction methods used for data are applied to the simulated event samples. Corrections are applied to match the selection efficiencies, energy and mass scales and resolutions of reconstructed simulated particles to those measured in data.

The ME generators are interfaced with different models for the simulation of the PS, hadronisation and the underlying event. Apart from events simulated with SHERPA [43], all MC samples use the EvtGEN programme [44] for the simulation of bottom and charm hadron decays. For all events interfaced with PYTHIA 8 [45] for the parton shower and hadronisation, the A14 tune [46] and the NNPDF2.3LO set of PDFs are employed. If not mentioned otherwise, the top-quark mass is set to 172.5 GeV.

3.1 Modelling of $t\bar{t}$ production in pQCD

3.1.1 Models based on Powheg v2 hvq + Pythia 8

The production of $t\bar{t}$ events is modelled using the Powheg Box v2 [47–51] generator with the hvq model (Powheg v2 hvq), which provides ME predictions for the production process $pp \rightarrow t\bar{t}$ at NLO accuracy in pQCD. The NNPDF3.0NLO [52] PDF set is used and the h_{damp} parameter, which effectively regulates the high p_T radiation against which the $t\bar{t}$ system recoils, is set to $1.5m_t$ [53]. The value of the strong coupling constant α_s is set to the value corresponding to the Z -boson mass scale, $\alpha_s(m_Z) = 0.119$. The renormalisation (μ_r) and factorisation (μ_f) scales are dynamic, using the functional form: $\sqrt{m_t^2 + p_T^2(t)}$. The ME predictions from Powheg v2 hvq are interfaced with Pythia 8.2. The value of the strong coupling constant in the final state shower of Pythia (α_s^{FSR}) is set to 0.127. ME corrections that approximate NLO QCD are enabled in Pythia for all emissions, compensating for the leading-order (LO) accuracy used in Powheg v2 hvq to simulate the top-quark decay. The p_T^{hard} parameter, which affects the matching of the PS to the ME calculation, is set to 0. The recoil for secondary and subsequent gluon emissions from the b -quark in the $t \rightarrow Wb$ vertex is assigned to the b -quark.² The early-resonance-decay parameter, which controls whether resonance decays can occur before or after colour reconnection (CR) happens in the simulation, is set such that resonance decays can only occur after CR.

Alternative pQCD Powheg v2 hvq $t\bar{t}$ samples obtained with different generator choices and settings are used to estimate systematic uncertainties related to the modelling of this dominant contribution. The details can be found in Section 8.2.1.

The $t\bar{t}$ samples are normalised to the cross-section prediction at next-to-next-to-leading order (NNLO) in QCD including the resummation of next-to-next-to-leading-logarithmic (NNLL) soft-gluon terms calculated using Top++ 2.0 [54–60]. For pp collisions at a centre-of-mass energy of $\sqrt{s} = 13$ TeV, this cross-section is calculated to be $\sigma(t\bar{t})_{\text{NNLO+NNLL}} = 833.9^{+37.4}_{-43.0}$ pb. In this calculation, the PDF4LHC21 PDF set [61] is used. The uncertainty is obtained by summing in quadrature the uncertainties related to the choice of PDF set, α_s , scale variations, and the top-quark mass uncertainty of ± 1 GeV. The $t\bar{t}$ normalisation is a free-floating parameter in the fit, hence the central cross-section value and its uncertainty only affect the pre-fit predictions, not the final result of the measurement.

Additionally, kinematic variables of the top-quark in the nominal and all alternative pQCD $t\bar{t}$ samples are corrected to more accurate differential predictions calculated at NNLO in α_s and NLO in α electroweak (α^{EW}) (NNLO-QCD+NLO-EW). The MATRIX programme [62] is used to obtain the predictions at NNLO in α_s , while HATHOR [63–66] is used to obtain the EW predictions at NLO. In both programmes, μ_r and μ_f are set to the dynamic scale values of $\frac{1}{2} \sum_{i \in \{t, \bar{t}\}} \sqrt{m_i^2 + p_{T,i}^2}$. The predictions allow for a two-dimensional reweighting in $(m_{t\bar{t}}, \cos \theta^*)$, where θ^* denotes the angle between the momentum of the top quark in the $t\bar{t}$ centre-of-mass frame and the momentum of the reconstructed $t\bar{t}$ system in the laboratory frame. They are provided in the ranges $340 \leq m_{t\bar{t}} \leq 3500$ GeV in bins of 10 GeV and $-1 \leq \cos \theta^* \leq +1$ in bins of 0.1. Since both the NNLO-QCD and NLO-EW predictions assume that both top quarks are on-shell, no reweighting can be applied for events with $m_{t\bar{t}} < 340$ GeV.

² This corresponds to the setting `recoilToColor=on` in the `TimeShower` class in Pythia.

3.1.2 Models based on Powheg v2 bb4l + Pythia 8

Another pQCD $t\bar{t}$ sample was generated using the $bb4\ell$ model implemented in Powheg Box Res [19, 67, 68] (Powheg v2 bb4l). This model includes off-shell and non-resonant contributions as well as exact spin correlations at NLO accuracy and simulates the inclusive production of $b\bar{b}\ell^+\ell^-v\bar{v}$ final states. In this way interference effects between $t\bar{t}$ and tW are taken into account. It also uses the new inverse-width correction described in Ref. [68] to correct for spurious width effects as well as improved resonance histories. The same settings as those used in the nominal $t\bar{t}$ sample are adopted for the renormalisation and factorisation scales, top-quark mass, PDF set, and value of α_s . The $bb4\ell$ predictions are interfaced with Pythia 8.3 using the A14 tune and the same PDF set as in the nominal sample. The $bb4\ell$ sample uses a recoil scheme in which the top-quark participates in the recoil to QCD radiation from b -quarks³ and the p_T^{maxMatch} and the p_T^{def} parameters are both set to 2. This sample is used to evaluate a systematic uncertainty related to the modelling of top-quark decays and off-shell effects (see Section 8). Additionally, it is used to provide an alternative baseline $t\bar{t}$ pQCD prediction, replacing the nominal Powheg v2 hvq + Pythia 8 setup, which is compared to the data in Appendix A. The detailed settings used to generate the sample are specified in Appendix B.

The Powheg v2 bb4l + Pythia 8 sample is normalised to the sum of the calculated higher-order cross-sections for $t\bar{t}$ (Section 3.1.1) and tW (Section 3.3) production. Kinematic variables of the sub-set of $t\bar{t}$ events which are identified as events with a doubly-resonant parton history [20] are corrected by reweighting them to the NNLO-QCD+NLO-EW predictions to which also the nominal Powheg v2 hvq + Pythia 8 sample is reweighted.

3.2 Modelling of $t\bar{t}$ quasi-bound-state effects

At the LHC, the dominant NRQCD contribution to the $t\bar{t}$ cross-section near the production threshold arises from the production of colour-singlet $t\bar{t}$ pairs via gluon fusion ($gg \rightarrow t\bar{t}$). Although top-antitop quark pairs produced in a colour-octet configuration experience a repulsive QCD potential and cannot form bound states, gluon exchange between the pair still leads to an enhancement of the cross-section at $m_{t\bar{t}}$ values slightly above $2 \cdot m_t$ via the Sommerfeld effect [1].

In the present analysis, NRQCD effects close to the production threshold, referred to as $t\bar{t}_{\text{NRQCD}}$, are modelled following the approach described in Ref. [28]. In this framework, the formation of colour-singlet states is described using the Green's function of non-relativistic QCD in the Coulomb gauge, which determines the momentum distribution of top quarks under the influence of the QCD potential. The Green's function is computed numerically by solving the Lippmann-Schwinger equation with input from the Fourier transform of the QCD potential [25, 69–71]. The result is used to reweight the MEs obtained at LO accuracy in pQCD for the production of a (potentially off-shell) colour-singlet $t\bar{t}$ pair in an S -wave configuration near the $t\bar{t}$ threshold, in order to generate a sample of quasi-bound-state $t\bar{t}$ events. The full production and decay to a six-body final state is generated using MADGRAPH 3.4.2 with the NNPDF3.0NLO PDF set and interfaced with Pythia 8.3. For consistency with the calculations in Ref. [28], which are used as input to the generation of this sample, the top-quark mass and width are set to 173 GeV and 1.49 GeV, respectively. Furthermore, we note that the value of the strong coupling constant in these calculations is set to $\alpha_s(m_Z) = 0.12$. As recommended in Ref. [28], the reweighting is applied only to events with $m_{t\bar{t}} < 350$ GeV and a top-quark momentum magnitude p^* in the $t\bar{t}$ centre-of-mass-frame of less than

³ This corresponds to the setting `recoilStrategyRF=3` in the `TimeShower` class in Pythia 8.312.

50 GeV. The overlap between this $t\bar{t}_{\text{NRQCD}}$ sample and the pQCD $t\bar{t}$ samples described in Sections 3.1.1 and 3.1.2 are assumed to be negligible, hence the double-counting corrections suggested in Ref. [28] are not applied [72].

The model described above provides a more complete description of $t\bar{t}$ quasi-bound-state formation than the simplified models introduced in Refs. [25, 26] which are used in Refs. [4, 24, 27] and compared in Ref. [29]. In these simplified models, $t\bar{t}$ quasi-bound states are represented either as a pseudo-scalar spin-singlet resonance or as a combination of scalar and pseudo-scalar resonances. These simplified models are motivated by the observation that the dominant S -wave contribution to $gg \rightarrow t\bar{t}$ production near the threshold arises mostly from the pseudo-scalar ${}^1S_0^{[1]}$ configuration [1, 15]. The contributions from states with higher total angular momentum J and colour-octet states are expected to be sub-dominant and are neglected in this model. In contrast, the nominal $t\bar{t}$ quasi-bound-state model, $t\bar{t}_{\text{NRQCD}}$, used in this analysis includes the full set of S -wave colour-singlet contributions, ${}^{2S+1}S_{J=L+S}^{[1]}$, incorporating both bound-state and scattering-state effects. The sample is normalised to a cross-section of 6.43 pb (including all decay channels), obtained from analytical calculations [25]. We note that no uncertainty estimate is currently available for this value, to the best of our knowledge. This calculated cross-section is larger than the 5.60 pb cross-section obtained directly from the MC simulation of this model, which does not include contributions from P -wave and colour-octet states. A branching ratio of 10.82% per lepton is assumed in the normalisation to the calculated inclusive cross-section.

To facilitate a direct comparison with the CMS analysis of Ref. [27], an alternative $t\bar{t}$ quasi-bound-state sample was generated using the simplified model of Ref. [25, 26] with a pseudo-scalar resonance $\eta_{t\bar{t}}$. The sample was produced in **MADGRAPH** 3.5.5 with the NNPDF3.0NLO PDF set. The $\eta_{t\bar{t}}$ mass is set to 343 GeV, in line with the expectation that the mass of the $t\bar{t}$ quasi-bound ground state is twice that of the top quark minus a binding energy of about 2 GeV [15, 25]. Its total width is set to 2.8 GeV, i.e. roughly twice that predicted for the top quark [8]. The full production and decay to the four-body $WbWb$ final state was generated. The PS and hadronisation are modelled with **PYTHIA** 8.3. As in the nominal NRQCD model, the sample cross-section is set to 6.43 pb.

3.3 Modelling of other Standard Model processes

Single-top tW associated production is modelled at NLO in pQCD using the **POWHEG Box v2** generator in the five-flavour scheme with the NNPDF3.0NLO PDF. The renormalisation and factorisation scales are dynamically set to $H_T/2$, where H_T is defined as the scalar sum of the p_T and invariant masses of the top quark and W boson [73]. The diagram-removal scheme [74] is employed to handle the interference with $t\bar{t}$ production [53]. The events are interfaced with **PYTHIA** 8.2 for the PS and hadronisation.

The inclusive cross-section is corrected to the theory prediction of $\sigma(tW) = 79.3^{+2.9}_{-2.8}$ pb, computed at NLO in QCD with the addition of third-order corrections of soft-gluon emissions by resummation of NNLL terms [75]. The top-quark mass is set to 172.5 GeV and the PDF4LHC21 PDF set is used. The quoted uncertainty includes variations in the scales μ_r , μ_f , and the PDFs.

Single-top t -channel production is modelled using **POWHEG Box v2** to provide ME predictions at NLO in pQCD using the four-flavour scheme with the corresponding NNPDF3.0NLO PDF set. The functional form of μ_r and μ_f is set to $4\sqrt{m_b^2 + p_{T,b}^2}$ following the recommendation of Ref. [76]. Top quarks are decayed at LO using **MADSPIN** [77, 78]. The events are interfaced with **PYTHIA** 8.2 for the PS and hadronisation. The

inclusive cross-section are corrected to the theory prediction calculated at NNLO in QCD with the MCFM program [79].

Single-top s -channel production are modelled using PowHEG Box v2 to provide MEs at NLO in pQCD in the five-flavour scheme with the NNPDF3.0NLO PDF set, while μ_r and μ_f are set to m_t . The events are interfaced with PYTHIA 8.2. The inclusive cross-section is corrected to the theory predictions calculated to approximate NNLO in QCD [80].

The production of a Z or W boson in association with jets ($V+jets$) are simulated with the SHERPA 2.2.11 and SHERPA 2.2.14 [43] generator using NLO MEs for up to two partons, and LO MEs for up to five partons calculated in the five-flavour scheme with the Comix [81] and OPENLOOPS [82–84] libraries. These predictions are matched with the SHERPA PS [85] using the MEPS@NLO prescription [86–89] and the set of tuned parameters developed by the SHERPA authors. The NNPDF3.0NNLO PDF set is used and the samples are normalised to the cross-section calculated at NNLO in pQCD [90]. The $Z+jets$ samples include contributions from virtual photon exchange and their interference with processes involving intermediate Z bosons.

Diboson (VV) production are simulated with SHERPA 2.2.1 or 2.2.2 depending on the process, including off-shell effects and Higgs-boson contributions where appropriate. Fully leptonic final states and semileptonic final states, where one boson decays leptonically and the other hadronically, were generated at NLO accuracy in pQCD for up to one additional parton and at LO accuracy in pQCD for up to three additional parton emissions. Samples for the loop-induced processes $gg \rightarrow VV$ were generated at LO accuracy for up to one additional parton emission for both fully leptonic and semileptonic final states. The ME calculations are matched and merged with the SHERPA PS based on Catani–Seymour dipole factorisation [81, 85] using the MEPS@NLO prescription [86–89]. The virtual QCD corrections are taken from the OPENLOOPS library [82–84]. The NNPDF3.0NNLO set of PDFs is used, along with the dedicated set of tuned parton-shower parameters developed by the SHERPA authors.

Other small backgrounds include the production of $t\bar{t}H$ events, modelled at NLO in pQCD using PowHEG Box v2 with the NNPDF3.0NLO PDF set, interfaced with PYTHIA 8.2 for the PS and hadronisation. The samples are normalised to the calculated total $t\bar{t}H$ cross-section at NLO QCD+EW accuracy [91]. The production of $t\bar{t}V$ events is modelled at NLO in pQCD using the MADGRAPH5_AMC@NLO 2.3.3 [92] generator with the NNPDF3.0NLO [52] PDF set, interfaced with PYTHIA 8.2. The samples are normalised to the calculated cross-sections for $t\bar{t} + Z$ and $t\bar{t} + W$ production, which are available at NLO in pQCD and NLO in the EW coupling [91]. The production of tWZ events is modelled at NLO in pQCD using MADGRAPH5_AMC@NLO 2.3.3 with the NNPDF3.0NLO PDF set, interfaced with PYTHIA 8.2. Finally, tZq events were generated at NLO in pQCD using MADGRAPH5_AMC@NLO 2.9.16 in the 4-flavour scheme and interfaced with PYTHIA 8.3.

4 Object reconstruction

Common event-quality criteria and object definitions are applied to all events considered for further analysis, including standard data-quality requirements to select data events with the detector in good operating condition [93]. Additional event selection criteria that are specific to the objects and kinematic variables of interest in dileptonic $t\bar{t}$ events are applied as described in Section 5.

Events are required to have at least one reconstructed pp interaction vertex with a minimum of two associated tracks with transverse momenta $p_T > 0.5$ GeV. The primary vertex is defined as the vertex with the highest sum of squared transverse momenta of associated tracks [94].

Muon candidates are reconstructed from matching tracks in the ID with tracks or track segments in the MS, refined through a global fit that uses the hits from both subdetectors [95]. They must have $p_T > 10$ GeV and $|\eta| < 2.5$, and satisfy a set of “Medium” identification criteria [96]. The longitudinal track impact parameter is required to satisfy $|z_0 \sin \theta| < 0.5$ mm and $|d_0/\sigma_{d_0}| < 3$ is required for the transverse impact parameter d_0 and its uncertainty σ_{d_0} . Muons isolation [96] is imposed by requiring that the sum of the transverse momenta of the tracks within a variable-radius cone around the muon direction, excluding the muon track, is less than 6% of the transverse momentum of the muon. The track isolation cone size is given by the minimum of $R = 10 \text{ GeV}/p_T^\mu$ and $R = 0.3$.

Electron candidates are reconstructed from energy deposits in the electromagnetic calorimeter matched to a charged-particle track in the ID [97, 98]. The track is required to be matched to the primary vertex by imposing the requirement $|z_0 \sin \theta| < 0.5$ mm and $|d_0/\sigma(d_0)| < 5$ on the longitudinal and transverse track impact parameters, respectively. Electron candidates are required to be within $|\eta_{\text{cluster}}| < 2.47$, excluding the transition region between the barrel and endcap calorimeters ($1.37 < |\eta_{\text{cluster}}| < 1.52$). They are further required to satisfy $p_T > 10$ GeV and the “TightLH” likelihood identification criteria [97]. The same variable-cone isolation requirement as for muons is imposed on electrons, with the exception that the maximum cone radius is set to 0.2.

Jets are reconstructed from particle-flow objects [99, 100] using the anti- k_t algorithm [101, 102] with a radius parameter $R = 0.4$. The energy scale of jets is calibrated using both simulation and data [100]. Contributions from pile-up are subtracted using the jet-area method [103]. Corrections are also applied to the simulation to bring the jet energy resolution in simulation into agreement with the jet energy resolution measured in data [100]. To suppress jets arising from pile-up, a jet-vertex-tagging (JVT) technique using a multivariate likelihood [104] is applied to jets with $p_T < 60$ GeV and $|\eta| < 2.4$, ensuring that selected jets are matched to the primary vertex. The jets used in this analysis are selected by requiring $p_T > 25$ GeV and $|\eta| < 2.5$.

Jets likely to contain decays of a b -hadron (henceforth called b -tagged) are identified using the ‘DL1r’ algorithm [105]. This algorithm is based on a multivariate classification technique with a deep neural network combining information from the impact parameters of tracks and topological properties of secondary and tertiary decay vertices reconstructed from the tracks associated to the jet. For this analysis, a working point (WP) corresponding to a b -tagging efficiency of 70 % is used. It provides rejection factors of approximately 380 for light-flavour jets and 10 for c -jets [105]. Efficiency and rejection correction factors are applied to the simulated jets, depending on whether they are b -tagged [106] or mistagged [107, 108]. The correction for b -jets is derived from $t\bar{t}$ events with final states containing two leptons, and the corrections are consistent with unity within uncertainties at the level of a few percent over most of the jet p_T range.

The reconstruction of the same energy deposits as multiple objects is resolved using an overlap removal procedure as described in the following. First, the closest selected jet within $\Delta R_y < 0.2$ of an electron is removed.⁴ Next, if an electron is found to be close to a jet ($\Delta R_y(\text{electron}, \text{jet}) < 0.4$), the electron is removed. Then jets that have fewer than three matched tracks are removed if they are within $\Delta R_y < 0.2$ of a muon candidate. Finally, muons that are within $0.2 < \Delta R_y < 0.4$ of a remaining jet are removed to suppress non-prompt muons.

⁴ The quantity ΔR_y is defined in analogy to the angular separation ΔR but using the rapidity y instead of the pseudorapidity η .

The missing transverse momentum, E_T^{miss} , is defined as the magnitude of the negative vectorial sum of the transverse momenta of all physics objects defined above. Tracks that are not associated with these physics objects but originate from the primary vertex are taken into account as a soft term [109].

5 Event selection and categorisation

Events with a detector signature consistent with that expected to arise from dileptonic $t\bar{t}$ events are selected by first imposing a set of loose preselection requirements. They are required to have fired one of the single-electron or single-muon triggers described in Section 3. Candidate events are further required to have exactly two charged leptons (electrons or muons) and at least two reconstructed jets. At least one of these leptons is required to have $p_T > 25/27/28$ GeV for data taken in 2015, 2016 and 2017+2018, respectively, and to match within $\Delta R < 0.15$ the lepton with the same flavour reconstructed by the trigger algorithm. Additionally, at least one of the jets is required to be b -tagged. Depending on the lepton flavour, events are referred to as ee , $\mu\mu$, or $e\mu$ events. The invariant mass of the reconstructed $t\bar{t}$ system (Section 6) must satisfy $m_{t\bar{t}} \leq 500$ GeV to prevent potential mis-modellings at high $m_{t\bar{t}}$ values from impacting the measurement.

The events are then further categorised into a set of signal regions (SRs) and two sets of control regions (CRs), used to estimate the background from Z +jets events (CR-Z) and from non-prompt and fake-lepton events (CR-Fakes).

Events in the SRs are required to contain two leptons with opposite electric charge, i.e. e^+e^- , $\mu^+\mu^-$, $e^+\mu^-$ or $e^-\mu^+$. Additionally, for ee and $\mu\mu$ events, the dilepton invariant mass, $m_{\ell\ell}$, is required to be greater than 15 GeV, not within the range 81–101 GeV around the Z -boson mass ($|m_{\ell\ell} - m_Z| \geq 10$ GeV) and the event is required to have $E_T^{\text{miss}} > 60$ GeV.

The CR-Z region comprises opposite-charge ee and $\mu\mu$ events compatible with the production of an on-shell Z boson. This is achieved by inverting the Z -boson mass-window requirement for the SRs. The same E_T^{miss} requirement as for the SRs is applied here. Finally, three CR-Fakes regions are constructed to contain same-charge ee , $\mu\mu$, and $e\mu$ events, respectively. The dilepton invariant mass is required to be greater than 15 GeV and not within the range 81–101 GeV around the Z -boson mass. No E_T^{miss} requirement is applied for the CR-Fakes regions. The contributions from quasi-bound-state formation to the overall $t\bar{t}$ contributions in the different CRs has been found to be negligible. The event selection requirements are summarised in Table 1.

Events in the SR are further categorised into nine angular regions based on the reconstructed values of the observables c_{hel} and c_{han} . The observable c_{hel} is the cosine of the angle between the charged-lepton directions after they have been Lorentz boosted into the $t\bar{t}$ centre-of-mass frame, and then separately into their parent top-quark and antitop-quark’s rest frames. It is the same angle used in the ATLAS and CMS $t\bar{t}$ entanglement analyses in $t\bar{t}$ dileptonic final states [3, 4]. Its distribution is expected to be linear, with a slope proportional to the trace of the spin correlation matrix of the $t\bar{t}$ pair. For a spin-singlet, the spins are maximally anti-correlated, and therefore the diagonal spin-correlations are -1 . Therefore, the distribution has a maximum slope for a spin-singlet state [2, 110]. The observable c_{han} is the cosine of the same angle, with a sign-flip in the component parallel to the top direction [111]. Its distribution has a maximum slope for a spin-triplet state. Both c_{hel} and c_{han} have a different shape in $t\bar{t}_{\text{NRQCD}}$ compared to pQCD $t\bar{t}$. For each angular observable, three bins of equal width are defined: $-1 \leq c_{\text{hel}} < -\frac{1}{3}$, $-\frac{1}{3} \leq c_{\text{hel}} < \frac{1}{3}$, $\frac{1}{3} \leq c_{\text{hel}} < 1$ (and similarly for c_{han}).

Table 1: Summary of event selection criteria for the SRs and CRs in the analysis. The letter ℓ refers to e and μ , and OSSF refers to a lepton pair with opposite charge and the same flavour.

SRs	CR-Z	CR-Fakes
$= 2\ell$ with $p_T(\ell) \geq 10$ GeV		
≥ 1 trigger-matched lepton with $p_T \geq 25/27/28$ GeV		
≥ 2 jets with $p_T \geq 25$ GeV		
≥ 1 b -tagged jet (70% efficiency WP)		
$m_{\ell\ell} \geq 15$ GeV		
$m_{t\bar{t}} \leq 500$ GeV		
$E_T^{\text{miss}} \geq 60$ GeV for OSSF events		—
$\ell^\pm \ell'^\mp$	$e^\pm e^\mp / \mu^\pm \mu^\mp$	$\ell^\pm \ell'^\pm$
$ m_{\ell\ell} - m_Z \geq 10$ GeV	$ m_{\ell\ell} - m_Z \leq 10$ GeV	$ m_{\ell\ell} - m_Z \geq 10$ GeV

6 Reconstruction of the top-antitop system

The reconstruction of the $t\bar{t}$ system from the two selected b -jet candidates, the charged leptons, and the \vec{p}_T^{miss} is based on the Ellipse Method [112], a geometric approach to analytically solve a system of constrained equations to obtain the four-vectors of the two neutrinos from the leptonically decaying W bosons. The two b -tagged jets associated with the decays of the top and antitop quarks are chosen from all selected hadronic jets. If more than two of them are b -tagged, the two leading b -tagged jets are selected. If there is only one b -tagged jet, the highest- p_T jet among the remaining untagged ones is selected.

The following kinematic constraints are imposed: (i) the invariant masses of the $\ell^+ \nu_\ell b$ and $\ell^- \bar{\nu}_\ell \bar{b}$ are equal to $m_t = 172.5$ GeV; (ii) the invariant masses of the $\ell^+ \nu_\ell$ and $\ell^- \bar{\nu}_\ell$ systems are equal to the W -boson mass of 80.4 GeV; and (iii) the two neutrinos ν_ℓ and $\bar{\nu}_\ell$ are the only source of \vec{p}_T^{miss} . The constrained equations are solved for both possible lepton- b -jet combinations in an event. The Ellipse Method can yield between zero and four solutions. If no solution is found for any of the lepton- b -jet combinations, the top-quark and W -boson mass values in the constrained equations are smeared assuming a Gaussian shape with mean $\mu = 172.5$ (80.379) GeV, and standard deviation $\sigma = 1.48$ (2.085) GeV for the masses and widths of the top quark (W boson), respectively. If there are multiple solutions, the solution with the smallest $m_{t\bar{t}}$ value is used.

The Ellipse Method provides a solution for about 95% of $t\bar{t}$ dilepton events for both the Powheg v2 hvq + Pythia 8 and $t\bar{t}_{\text{NRQCD}}$ samples in the SR. Events where no solution was found are discarded. The fraction of events without a solution is consistent between data and simulation. The resolution of the reconstructed $m_{t\bar{t}}$, $m_{t\bar{t}}^{\text{reco}}$, is taken as the standard deviation of the distribution of the quantity $(|m_{t\bar{t}}^{\text{reco}} - m_{t\bar{t}}^{\text{true}}|)/m_{t\bar{t}}^{\text{true}}$, where $m_{t\bar{t}}^{\text{true}}$ is the parton-level $m_{t\bar{t}}$. It is evaluated in bins of the $m_{t\bar{t}}^{\text{true}}$ distribution, each with a width of 5 GeV, and is about 22% at the $t\bar{t}$ threshold and improves to about 18% for $m_{t\bar{t}}^{\text{true}} \approx 500$ GeV.

7 Estimation of other Standard Model processes

After applying all selection requirements, the SRs are expected to contain about 700,000 $t\bar{t}$ events based on the baseline Powheg v2 hvq + Pythia 8 model before the profile-likelihood fit to data. This number

increases by around 6,900 events for the extended sample, which includes in addition the predictions for $t\bar{t}$ quasi-bound-state formation using the normalised nominal sample described in Section 3.1. Smaller background contributions arise from various sources. The largest non- $t\bar{t}$ background is the production of a single top-quark in addition with a W boson (tW), with a 4% contribution to the total event yields. Rare processes involving top quarks, labelled $t + X$ and including e.g. $t\bar{t} + Z$, $t\bar{t} + W$, $t\bar{t} + H$ and their single-top counterparts, as well as diboson ($VV+jets$) production account for 0.3% and 0.2% of the total pre-fit event yields, respectively. These processes are all taken from MC simulation.

Two additional background components are estimated using MC simulations corrected with data from dedicated control regions. The background from $Z+jets$ production contributes to the SRs mostly via non-resonant Drell-Yan production and also on-shell via $Z \rightarrow \tau^+\tau^-$ where the τ -leptons decay leptonically. This contribution represents 0.8% of the total number of events in the SRs. The $Z+jets$ process is separated into three components according to the flavour of the additional leading jet in the event: $Z + b$, $Z + c$ and $Z + \text{light}$. The $Z + b$ component is dominant and subject to significant modeling uncertainties in this region of phase space [113]. A normalisation factor for $Z + b$ is therefore obtained in the profile-likelihood fit from the dedicated CR-Z regions (Section 5). The $Z + c$ and $Z + \text{light}$ components are taken directly from the MC simulations and assigned conservative normalisation uncertainties (Section 8).

Another small background component arises from processes with at least one fake or non-prompt lepton that satisfies the lepton identification and isolation criteria (Section 4). This is mostly $t\bar{t}$ production with one top quark decaying hadronically and the other leptonically, as well as single-top and $W+jets$ production. It contributes around 1.5% to the total event yield in the SRs. The two main sources of fake leptons are electrons from photon conversions, with a contribution of 30-40% to the total fake-lepton background, as well as electrons and muons from heavy-flavour hadron decays, accounting for most of the remaining fake-lepton events. Electrons originating from photon conversions are characterized by a softer transverse momentum spectrum compared to those produced from heavy-flavour hadron decays. The $m_{t\bar{t}}$ shapes of this background in the SRs are taken from MC simulations for the relevant processes. Its normalisation is determined by fitting the distributions of the trailing lepton p_T to data in the fake-lepton-enriched CR-Fakes regions (Section 5). Three independent normalisation factors, e -HF-fakes, μ -HF-fakes, and e -PhConv-fakes, are defined, depending on whether the fake lepton is an electron or a muon from a heavy-flavour decay or an electron arising from a photon conversion, respectively. They are free-floating in the final profile-likelihood fit.

8 Systematic uncertainties

A broad range of experimental and modeling uncertainties are considered for PowHEG v2 hvq + PYTHIA 8, $t\bar{t}_{\text{NRQCD}}$, and non- $t\bar{t}$ processes. These can affect both the shape and the normalisation of the $m_{t\bar{t}}$ spectra in the different SRs.

8.1 Experimental uncertainties

Experimental uncertainties cover reconstructed objects, pile-up modeling, and luminosity. Most uncertainties affect both shape and normalisation, while for the luminosity uncertainty only normalisation effects are considered. They are applied to all processes, with details provided below.

Jets: The dominant jet-related uncertainties are uncertainties in the jet-energy scale (JES) and resolution (JER) [100]. These include uncertainties related to the jet flavour composition [114], punch-through, calorimeter response to different jet flavours, as well as pile-up effects. An uncertainty in the JVT efficiency is also considered [104].

b-tagging: Uncertainties in the b -tagging efficiency and mis-tag rates for c - and light-flavour jets, derived from dedicated measurements in flavour-enriched data and MC samples [106, 107, 115], are included.

Leptons: Uncertainties in electron and muon trigger, identification, isolation and reconstruction efficiencies as well as energy scale and resolution uncertainties are also included. They are derived from dedicated analyses using data control samples [95–98, 116, 117].

E_T^{miss} : Object-related uncertainties are propagated to E_T^{miss} [118], with additional contributions from the scale and resolution of tracks not associated with leptons or jets [119].

Pile-up: Uncertainties in the pile-up reweighting are included, accounting for differences between predicted and measured values of the inelastic cross-sections and of the average number of interactions per bunch crossing [104].

Luminosity: A 0.83% normalisation uncertainty in the integrated luminosity [34] is applied to all samples except the fake-lepton and Z +jets backgrounds, which are estimated from data.

8.2 Modelling uncertainties

8.2.1 pQCD $t\bar{t}$ production

An extensive range of uncertainties related to the MC modelling of pQCD $t\bar{t}$ production using PowHEG v2 hvq + PYTHIA 8 is taken into account. They include the following uncertainties in the NNLO-QCD+NLO-EW prediction to which the generated nominal and alternative samples are reweighted.

NNLO-QCD scales: The effect of missing higher-order corrections is estimated by reweighting the PowHEG v2 hvq + PYTHIA 8 sample to alternative NNLO-QCD+NLO-EW predictions obtained by varying μ_r and μ_f by factors of 2 and 0.5 and taking the envelope of the resulting variations. All μ_r and μ_f combinations are considered except for those for which $\mu_r = 2, \mu_f = 0.5$ and vice versa, see Ref. [55].

NLO-EW correction scheme: An additional uncertainty comes from the difference between additive and multiplicative schemes used to combine NLO EW and NNLO pQCD corrections [65].

The impact of an additional uncertainty in the NLO electroweak (EW) correction, associated with a variation of the top-quark Yukawa coupling by $\pm 10\%$ [120], was evaluated and found to have a negligible effect on the results presented in Section 9. In the SM, the top-quark mass and its Yukawa coupling are intrinsically correlated. Since an uncertainty on the top-quark mass is explicitly accounted for (see below), no additional uncertainty is assigned to the Yukawa coupling.

Uncertainties related to generator and parameter choices in the nominal PowHEG v2 hvq + PYTHIA 8 sample are also taken into account in the fit. They are described in the following. In the case of one-sided uncertainties, it is assumed that the effect is symmetric to obtain effective *up* and *down* variations compared to the nominal prediction.

Top-quark mass: The effect of the top-quark mass uncertainty is evaluated by comparing the $m_{t\bar{t}}$ spectra obtained using the nominal sample to those generated with top quark masses of 172.0 and 173.0 GeV.

Top-quark decay and off-shell effects: An uncertainty associated with the modelling of top-quark decays and off-shell effects arises from differences in the treatment of spin correlations in $t\bar{t}$ production across generators. This uncertainty is assessed by comparing the sum of the $t\bar{t}$ sample which uses the top quark in the recoil scheme and the tW sample to an alternative sample generated with the PowHeg v2 bb41 + Pythia 8 setup (Section 3).

PDF + α_s : PDF uncertainties are evaluated using the 30 eigenvectors in the PDF4LHC15 [121] prescription, symmetrising the full difference between the nominal PDF4LHC weight and the variation for each eigenvector. Alternative PDF sets corresponding to different α_s values of 0.117 and 0.119 are also included.

PS and hadronisation: The PS and hadronisation model uncertainty is estimated by comparing the nominal predictions to those obtained from a sample generated at NLO in pQCD with PowHeg Box v2 using the same settings as the nominal PowHeg sample for the hard scattering but interfaced with HERWIG 7.2 [122, 123], using the default set of tuned parameters [123] and the MMHT2014LO PDF set [124].

ME-PS matching: The ME-PS matching uncertainty is estimated by comparing the nominal sample to one with the same settings but using $p_T^{\text{hard}} = 1$ instead of 0 in Pythia [125].

h_{damp} setting: The uncertainty related to the modelling of high- p_T radiation is estimated by comparing the nominal sample to one with the h_{damp} parameter increased by a factor of 2 [53].

Initial-state radiation (ISR): Uncertainties in the ISR modelling are estimated according to the VAR 3C set of parameters which are part of the A14 tune [46].

Final-state radiation (FSR): Similarly, the uncertainty related to FSR is assessed by varying μ_r for final-state parton-shower emissions up and down by a factor of two.

Recoil scheme: In simulating QCD radiation from b -quarks in top-quark decay, there is an ambiguity in the choice of the recoil particle after the first gluon emission [126]. This affects out-of-cone radiation for b -tagged jets and hence the reconstructed top mass. The associated uncertainty is evaluated using a Pythia sample where the top quark participates in the recoil [127].

Colour reconnection: The colour reconnection uncertainty is estimated using two samples. In the ‘QCD-based’ model (CR1) the formation of dipoles containing three quarks is enhanced, leading to increased baryon production, while in the ‘gluon-move’ model (CR2) only the gluons are considered for the reconnection. To estimate the associated systematic effect, a third sample (CR0) with the nominal multiple parton interaction (MPI) model and a tune matching that of CR1 and CR2 [128, 129], respectively, is used.

Underlying event: Uncertainties related to the modelling of the underlying event and MPI are evaluated with two samples where the settings for the α_s value used in the MPI and colour-reconnection range of the proton beam remnants are changed according to the VAR 1 set of parameters which are part of the A14 tune [46].

The alternative MC samples used to define the modelling uncertainties in the nominal PowHeg v2 hvq + Pythia 8 simulation are each reweighted to the NNLO-QCD+NLO-EW predictions, with two exceptions: no dedicated NNLO-QCD+NLO-EW weights are derived for the samples with alternative m_t values to avoid underestimating this uncertainty by reweighting it to a higher-order prediction evaluated at a fixed top-quark mass $m_t = 172.5$ GeV. Instead, the weights derived for the nominal sample are applied to these samples. The same approach is used for the uncertainty in the choice of the PS+hadronisation

model as it covers modelling differences that are not expected to affect the ME dynamics relevant for the reweighting.

8.2.2 Quasi-bound-state effects

Modelling uncertainties are taken into account for $t\bar{t}$ quasi-bound-state production. They are applied to both the main model as well as the simplified model discussed in Appendix C.

Scale variations: The effect of missing higher-order corrections is estimated by varying μ_r and μ_f by factors of 2 and 0.5, and is treated as uncorrelated with those in the pQCD $t\bar{t}$ sample due to different orders at which the processes are modelled. The normalization shift for μ_r (μ_f) is 23% (2%), and the overall impact from acceptance changes is 0.5%.

PDF + α_s : Uncertainties related to the choice of PDF set and the value of α_s in the nominal PDF set are applied according to the same approach used for the $t\bar{t}$ pQCD sample as described in Section 8.2.1, except that the more recent PDF4LHC21 prescription is used.

PS and hadronisation, ISR, FSR: Uncertainties related to the modelling of the PS and hadronisation as well as ISR and FSR are obtained at the particle level. They are evaluated in the same way as the equivalent uncertainties in the $t\bar{t}$ pQCD sample. They are propagated to reconstructed events via an event-by-event reweighting.

8.2.3 Other Standard Model processes

MC modelling uncertainties for sub-dominant background processes are detailed below. For tW production, both shape and normalization effects are included. For other minor backgrounds, conservative normalization uncertainties are used, with the exception of the fake-lepton background, whose normalisation is obtained from the fit.

Single top quark: The main single-top modelling uncertainty stems from interference and overlap with $t\bar{t}$, estimated by comparing the nominal tW sample using diagram-removal to an alternative sample with diagram-subtraction [53, 74] under identical settings. Uncertainties from PS and hadronisation model, ME-PS matching (p_T^{hard}), h_{damp} , and top-quark mass are estimated as in the pQCD $t\bar{t}$ sample. A 4% normalization uncertainty reflects the tW cross-section uncertainty used to normalize the MC samples [130].

$t\bar{t} + b$ and $t\bar{t} + c$: Events in which a $t\bar{t}$ pair is produced in association with an additional b - or c -quark, referred to as $t\bar{t} + b$ and $t\bar{t} + c$, respectively, are identified within the nominal pQCD $t\bar{t}$ sample using particle-level information. The relative contribution of the $t\bar{t} + b$ ($t\bar{t} + c$) subsample is varied by 20% (40%) to account for the uncertainties in the relative cross-sections of these processes.

$t\bar{t} + X$: A conservative 50% normalisation uncertainty is applied to the $t\bar{t} + X$ ($X = W, Z, H$) and the tiny $t+X$ background components.

Diboson: A conservative 50% normalization uncertainty is applied to the diboson background to cover possible mismodelling of extra and heavy-flavour jets [131, 132].

Z+jets: For Z +jets, the $Z + b$ normalisation is a free parameter of the fit, while 50% normalisation uncertainties are applied to $Z + c$ and $Z + \text{light}$ components.

9 Results

The agreement between the data and the predictions of the baseline model without quasi-bound-state effects included and the extended models for $t\bar{t}$ production that include quasi-bound-state effects is quantified using a binned profile-likelihood fit [133] of the expected $m_{t\bar{t}}$ distributions to data in the nine SRs, as well as the one CR-Z and the three CR-Fakes control regions. In total, 13 orthogonal regions are included in the fit.

The templates used in the fit are obtained from the MC simulations described in Section 3. In the SRs and CR-Z, the $m_{t\bar{t}}$ distributions in the range 300 – 500 GeV are considered. The range and binning are chosen such that the template contains four bins with equal width of 50 GeV for $m_{t\bar{t}} < 500$ GeV. In the CR-Fakes regions, the fitted distribution is that of the trailing lepton p_T with three bins: [10, 20, 40, 200] GeV.

Six normalisation factors defined as $\mu = \sigma_{meas.}/\sigma_{theory}$ for the $t\bar{t}_{\text{NRQCD}}$, $t\bar{t}$, e -HF-fakes, e -PhConv-fakes, μ -HF-fakes, and $Z + b$ processes are extracted simultaneously from the fit.

Here and in the following the SRs are numbered from 1 to 9, corresponding to the bins shown in Fig. 1.

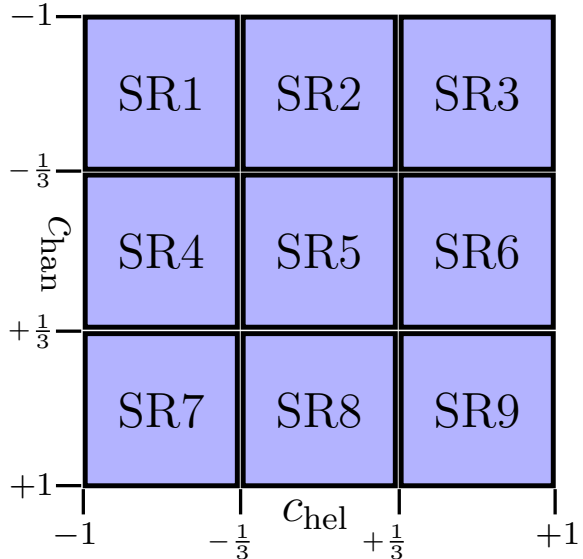


Figure 1: Definition of the nine signal regions based on the angular variables c_{hel} and c_{han} .

The $m_{t\bar{t}}$ distributions in the nine SRs before the fit are shown in Figure 2, using the numbering scheme defined above from left to right.

An excess of events compared to the baseline PowHEG v2 hvq + PYTHIA 8 model, without $t\bar{t}_{\text{NRQCD}}$ effects included, is visible in all SRs at low values of $m_{t\bar{t}}$, most notably in SRs 5, 6, 8, and 9, i.e. the SRs characterised by larger values of c_{hel} and c_{han} . In general, the excess is in better agreement with the predictions of the extended model that includes the quasi-bound-state $t\bar{t}_{\text{NRQCD}}$ predictions (normalised to 6.43 pb). In SRs 8 and 9, the observed data yields in the lowest bin in $m_{t\bar{t}}$ notably exceed those predicted in the $t\bar{t}_{\text{NRQCD}}$ model.

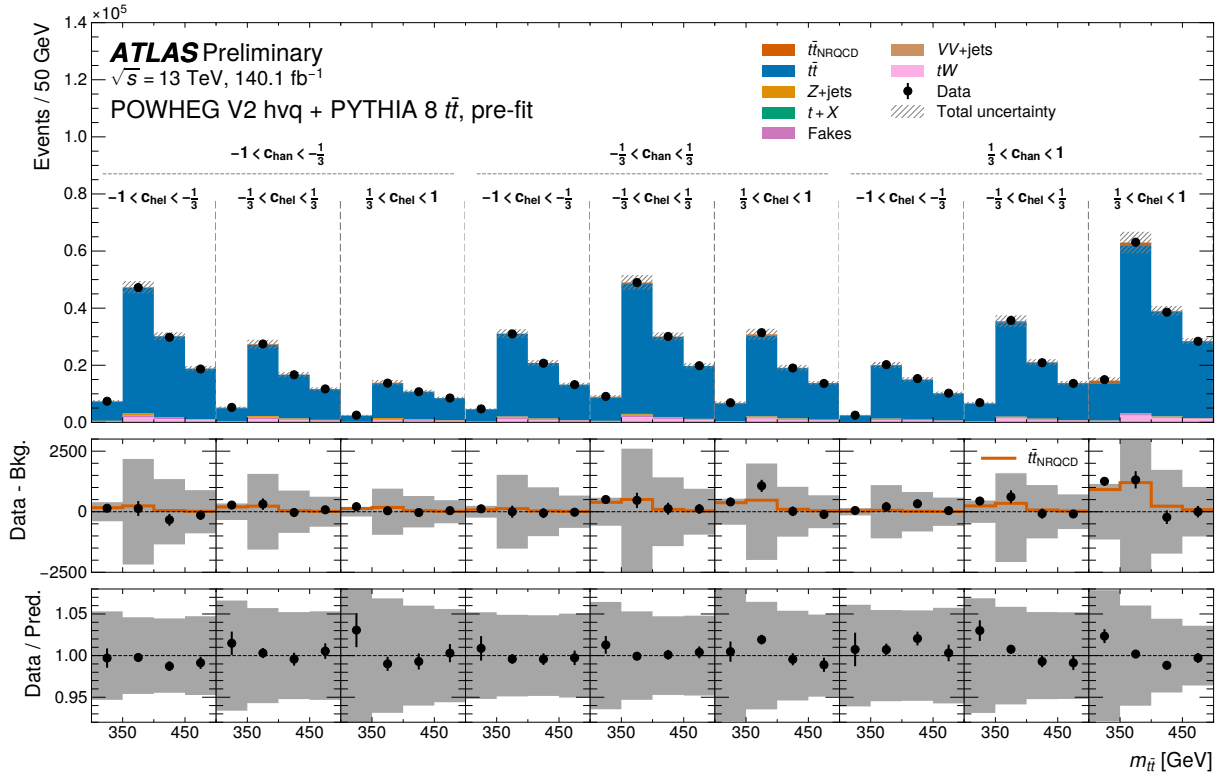


Figure 2: Pre-fit distributions of $m_{t\bar{t}}$ in the nine SRs (upper panel), together with a comparison between the $t\bar{t}$ quasi-bound-state prediction and the data, from which the pQCD $t\bar{t}$ contribution and background processes have been subtracted (middle panel), and the ratio of the data and the extended $t\bar{t}$ model including $t\bar{t}_{\text{NRQCD}}$ contributions (lower panel). The error bars on the data markers represent the statistical uncertainty of the measurement, while the gray hashed and shaded bands represent the total systematic uncertainty in the prediction.

9.1 Treatment of systematic uncertainties

Systematic uncertainties, including those arising from the limited size of the MC samples used to model the background processes, are included in the likelihood function by means of constrained nuisance parameters (NPs), allowing for adjustments in the shape and normalisation of all histogram templates.

All experimental uncertainties are treated as fully correlated across samples and the analysis regions entering the fit. The modelling uncertainties are treated as uncorrelated between the $t\bar{t}$ and non- $t\bar{t}$ samples but, in the majority of cases, as fully correlated between the analysis regions.

In the case of NPs that are strongly constrained to less than 50% of their pre-fit uncertainty, the original systematic variation is treated as partially (50%) correlated between the different regions (SRs and CRs). This is achieved by splitting it into one part, obtained from the original systematic variation scaled by a factor of $1/\sqrt{2}$, which is treated as fully correlated across SRs, and N parts obtained in the same way but treated as fully uncorrelated across the $N = 13$ regions entering the fit. This approach was found to only slightly reduce the sensitivity of the measurement and to have a negligible effect on the normalisation factors for the backgrounds, while significantly reducing the NP constraints in the SRs and improving the Goodness-of-Fit value. The Goodness-of-Fit value is calculated using a saturated model [134] and quantifies the agreement between the data and the model under consideration, accounting for the penalties

arising from shifts in the nuisance parameters during the fit. A high Goodness-of-Fit value indicates good agreement between the data and the model with minimal shifts in the nuisance parameters.

The partial decorrelation approach is applied to the uncertainty in the PS and the uncertainty in the modelling of top-quark decays and off-shell effects. Alternative correlation approaches for these two uncertainties have been tested, including a full correlation across all regions, a full decorrelation between the nine SRs, and a splitting of the related NPs by their shape and acceptance components. Additionally, the partial decorrelation approach was tested for the slightly less constrained NPs, such as those related to the choice of the recoil-to-top setting. For most alternative correlation schemes, the differences in the fitted normalisation factors compared to the nominal setup were negligible, and the impact on the associated uncertainties was small. Treating all NPs as fully correlated across regions yields a 15% reduction of the uncertainty in the normalisation factor for the $t\bar{t}_{\text{NRQCD}}$ process compared to the nominal correlation scheme, with a negligible change in the fitted central value.

9.2 Fit results

The cross-section for the $t\bar{t}$ quasi-bound-state contribution extracted from the fit with free-floating signal normalisation $\mu(t\bar{t}_{\text{NRQCD}})$ is

$$\sigma(t\bar{t}_{\text{NRQCD}}) = 9.0 \pm 1.3 \text{ pb} = 9.0 \pm 1.2 \text{ (stat.)} \pm 0.6 \text{ (syst.) pb},$$

which is $(40 \pm 20)\%$ larger than the predicted value of 6.43 pb. As stated in Section 3.2, no uncertainty estimate is available for this value. The baseline model without quasi-bound-state contributions is rejected with an observed (expected) significance of 7.7σ (5.7σ).

The other normalisation factors extracted from the fit with free-floating $t\bar{t}_{\text{NRQCD}}$ contribution are

$$\begin{aligned}\mu(t\bar{t}) &= 0.98 \pm 0.03 \\ \mu(e\text{-HF-fakes}) &= 1.03 \pm 0.07 \\ \mu(e\text{-PhConv-fakes}) &= 1.03^{+0.15}_{-0.23} \\ \mu(\mu\text{-HF-fakes}) &= 1.18 \pm 0.04 \\ \mu(Z + b) &= 0.69^{+0.39}_{-0.32}\end{aligned}$$

As a cross-check, the normalisation factors were also fitted separately for three different data-taking periods during LHC Run 2: 2015+2016, 2017, 2018, and separately in ee , $e\mu$, and $\mu\mu$ events. In all cases, the results agree with those derived from the nominal fit within their uncertainties.

The $m_{t\bar{t}}$ distributions in the nine SRs after this fit are shown in Figure 3. Good agreement for the extended model is observed after the fit, with significantly reduced NP shifts compared to the fit without the quasi-bound-state contribution. Accordingly, the Goodness-of-Fit value degrades from 0.93 in the fit with the extended model to $7 \cdot 10^{-5}$ when the quasi-bound-state is omitted. The post-fit distributions for the trailing-lepton p_T in the CR-Fakes regions and $m_{t\bar{t}}$ in the CR-Z region can be found in Appendix D. The data agree with the predictions in all CRs.

Figure 4 shows the impact of individual sources of uncertainty, as well as the shift and the constraints of the associated NPs with the largest impact on the extracted $t\bar{t}_{\text{NRQCD}}$ cross-section. The impact of all sources of uncertainty is summarised in Table 2. Apart from the dominant statistical uncertainties, the measurement

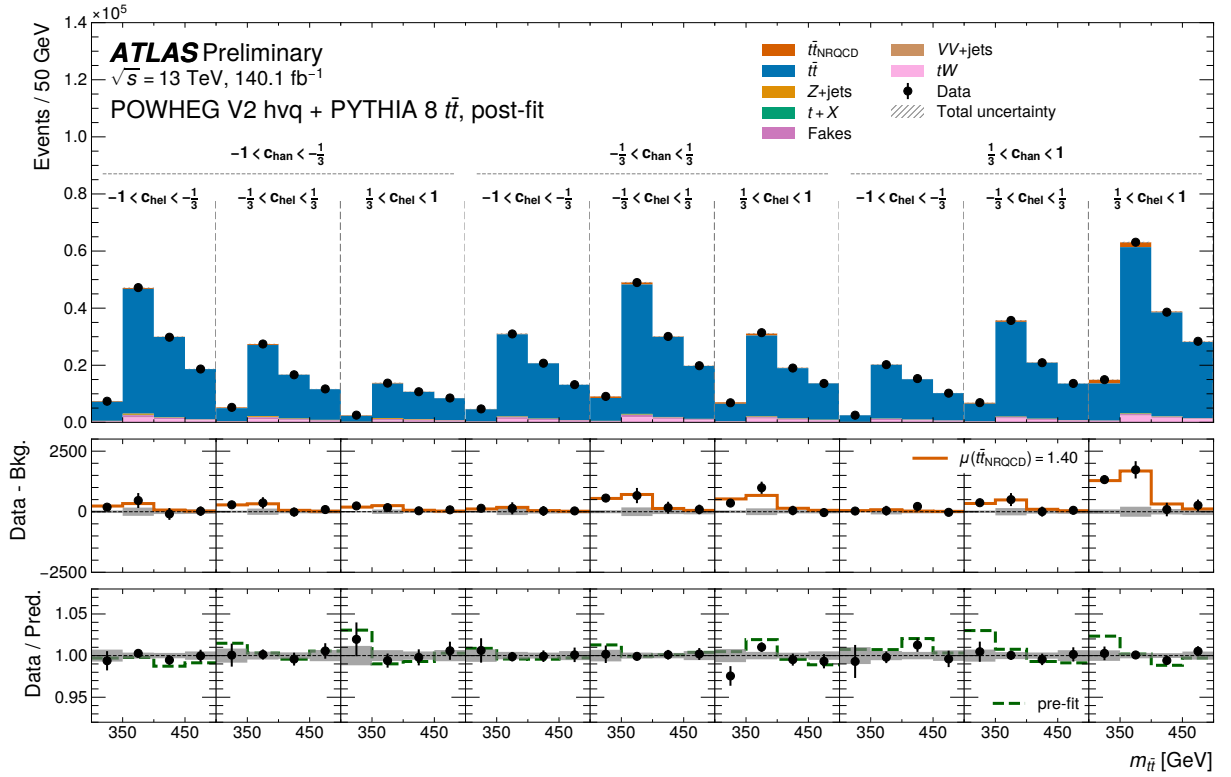


Figure 3: Post-fit distributions of $m_{t\bar{t}}$ in the nine SRs (upper panel), together with a comparison between the $t\bar{t}$ quasi-bound-state prediction and the data, from which the pQCD $t\bar{t}$ contribution and background processes have been subtracted (middle panel), and the ratio of the data and the extended $t\bar{t}$ model including $t\bar{t}_{\text{NRQCD}}$ contributions (lower panel). The error bars on the data markers represent the statistical uncertainty of the measurement, while the gray hashed and shaded bands represent the total systematic uncertainty in the prediction. The dashed line represents the data/MC ratio before the fit.

precision is limited by signal and background modelling uncertainties. For the signal, the dominant effect is the parton-shower and hadronisation uncertainty.

The strongest constraints on NPs are observed for uncertainties related to the $t\bar{t}$ modelling, in particular the fully correlated component of the top-quark decay and off-shell effects (0.49), its uncorrelated component in SR 2 (0.46), and the PS uncertainty in SR 2 (0.52). Among the experimental uncertainties, the jet pileup ρ topology is the most constrained at 0.80. It accounts for the difference in the average pile-up energy density ρ between the dijet and $t\bar{t}$ topologies that affect the area-based pile-up subtraction applied to jets and hence the measured JES [100]. Among these highest ranked uncertainties the NPs related to the uncertainty in the NNLO-QCD reweighting and the uncertainty in the modelling of the $t\bar{t}$ decay and off-shell effects (NP for SR 7) are shifted upwards by approximately 0.5 pre-fit standard deviations. These uncertainties have a large impact in the lowest $m_{t\bar{t}}$ bins where the pre-fit excess is observed in the data.

The large impact of the uncertainty associated with the modelling of top-quark decays and off-shell effects can be explained via a comparison of the $m_{t\bar{t}}$ distributions in the different SRs obtained with Powheg v2 bb41 + Pythia 8 and Powheg v2 hvq + Pythia 8, respectively. In Figure 5, the ratio of these two predictions is compared with the ratio between the Powheg v2 hvq + Pythia 8 + $t\bar{t}_{\text{NRQCD}}$ model and the Powheg v2 hvq + Pythia 8 model without quasi-bound-state contributions. The shape predicted by the

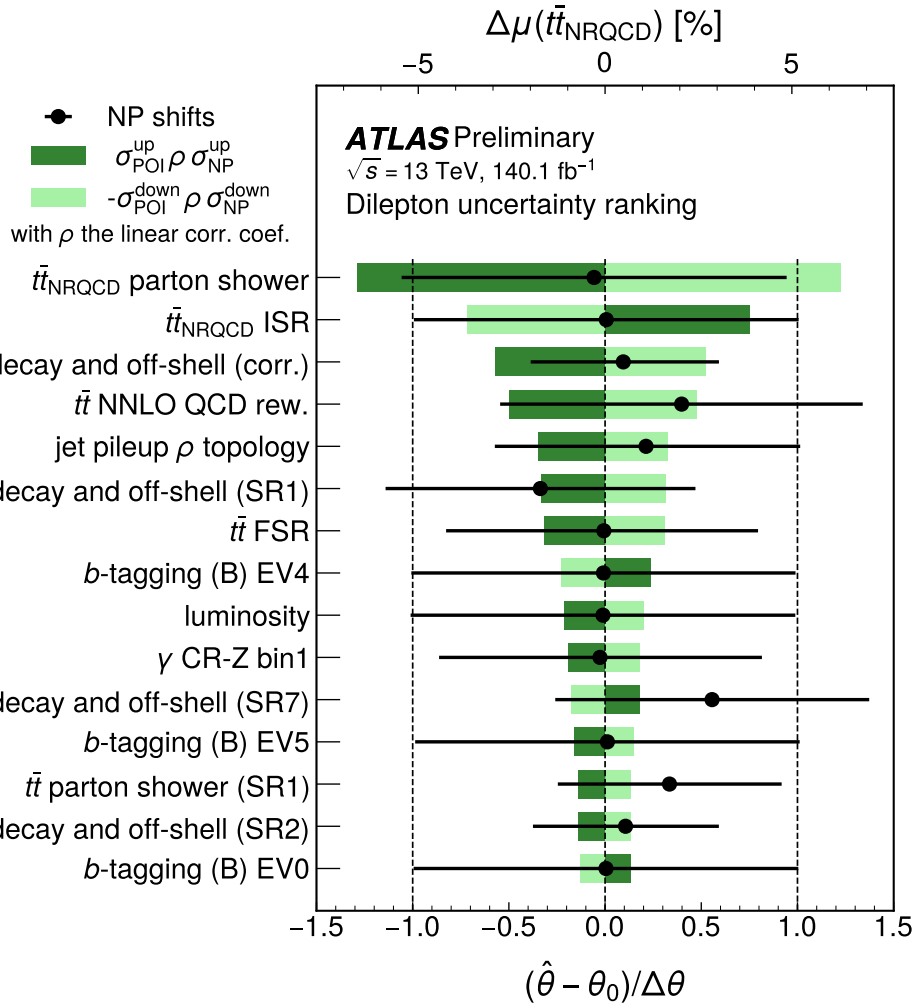


Figure 4: Ranking of the 15 most impactful individual NPs on $\mu(\bar{t}\bar{t}_{\text{NRQCD}})$ in the profile-likelihood fit with free-floating $\mu(\bar{t}\bar{t}_{\text{NRQCD}})$. The covariance-matrix approximation of the shifted observables method is used to evaluate the impact of a given NP [135]. The impact is taken as the corresponding off-diagonal element of the fit covariance matrix divided by its pre-fit uncertainty and is given in percent on the upper scale. The black marker shows the shifts of the NPs relative to the nominal value θ_0 . They are shown together with their corresponding uncertainty on the lower scale. The SR numbers correspond to the bins introduced in Fig. 1. For the flavour-tagging uncertainties, individual eigenvariations (EVs) are shown.

Table 2: Breakdown of the total uncertainty in the fitted normalisation factor $\mu(t\bar{t}_{\text{NRQCD}})$ into its statistical and systematic components. The impact for a given NP is taken as the corresponding off-diagonal element of the fit covariance matrix divided by its pre-fit uncertainty. The impact of a group of NPs is obtained by summing the impacts of all NPs in this category in quadrature. The total systematic uncertainty is obtained by summing in quadrature the impacts of all NPs. The statistical uncertainty in the signal strength is calculated based on the requirement that the sum in quadrature of the statistical uncertainty and the total systematic uncertainty must yield the total uncertainty in the signal strength as obtained from the initial profile-likelihood fit in which all NPs are allowed to float. The category "Instrumental (other)" takes into account the uncertainty in the luminosity, pileup reweighting and jet-vertex tagger efficiency.

Category	Impact
$t\bar{t}_{\text{NRQCD}}$ modelling	5.3%
$t\bar{t}$ modelling	3.5%
Jet energy scale (pileup)	1.3%
b -tagging	1.2%
Instrumental (other)	0.9%
Limited MC statistics	0.7%
Jet energy scale (flavour)	0.5%
Background normalisations	0.4%
tW modelling	0.4%
Jet energy scale (η inter-calibration)	0.4%
Jet energy scale (other)	0.3%
Jet energy resolution	0.3%
Leptons	0.2%
Total syst. uncertainties	6.8%
Total stat. uncertainties	13%

POWHEG v2 bb41 + PYTHIA 8 model is more similar to that of the extended model than to the baseline model without quasi-bound-state contributions at low values of $m_{t\bar{t}}$. At higher values of $m_{t\bar{t}}$, however, the predictions of the **POWHEG v2 bb41 + PYTHIA 8** model differ from those of the extended **POWHEG v2 hvq + PYTHIA 8 + $t\bar{t}_{\text{NRQCD}}$** in that the former predicts higher yields compared to **POWHEG v2 hvq + PYTHIA 8**, which is not the case for the **POWHEG v2 hvq + PYTHIA 8 + $t\bar{t}_{\text{NRQCD}}$** model.

The predictions for the alternative extended **POWHEG v2 hvq + PYTHIA 8 + $\eta_{t\bar{t}}$** model and the alternative baseline model using **HERWIG** instead of **PYTHIA** for the PS and hadronisation are also shown in Figure 5. The two extended models exhibit qualitatively similar behaviour, with the $t\bar{t}_{\text{NRQCD}}$ model yielding a slightly larger excess of events relative to the **POWHEG v2 hvq + PYTHIA 8** prediction in the lowest $m_{t\bar{t}}$ bin than the $\eta_{t\bar{t}}$ model. The **HERWIG**-based baseline predicts lower event yields and reduced spin correlations relative to the nominal **POWHEG v2 hvq + PYTHIA 8** model. In contrast, both extended models predict enhanced event yields and stronger spin correlations. Further plots comparing the pre-fit predictions of these $t\bar{t}$ models are included in Appendix F.

The results with the simplified model of Refs. [25, 26] are included in Appendix C. Using this setup, a larger cross section of 13.4 ± 1.9 pb is obtained, with an observed (expected) significance of 7.8σ (4.0σ).

An alternative set of results using Powheg v2 bb41 + Pythia 8 for the pQCD $t\bar{t}$ prediction is summarised in Appendix A. With this setup, a lower cross section of 4.2 ± 1.0 pb is measured, with a significance of 4.3σ observed (6.3σ expected). The goodness-of-fit value obtained for the Powheg v2 bb41 + Pythia 8 + $t\bar{t}_{\text{NRQCD}}$ model is 0.54 and larger NP shifts are observed after the fit, indicating an overall poorer agreement of this model with the data. The Powheg v2 bb41 + Pythia 8 pQCD setup is still under scrutiny in ATLAS, in consultation with the generator authors. Dedicated efforts to define the best nominal settings and a corresponding systematic model are currently ongoing. This includes the implementation of higher-order corrections to the $t\bar{t}$ and tW contributions, which currently relies on the identification of $t\bar{t}$ events via the parton history at LO accuracy in the relevant couplings (Section 3.1.2). Further input from the theory community is needed to identify the most suitable setup. Nevertheless, these alternative fit setups demonstrate that neither of the two baseline models of pQCD $t\bar{t}$ production describes the data well, unless a model of $t\bar{t}$ quasi-bound-state formation is included.

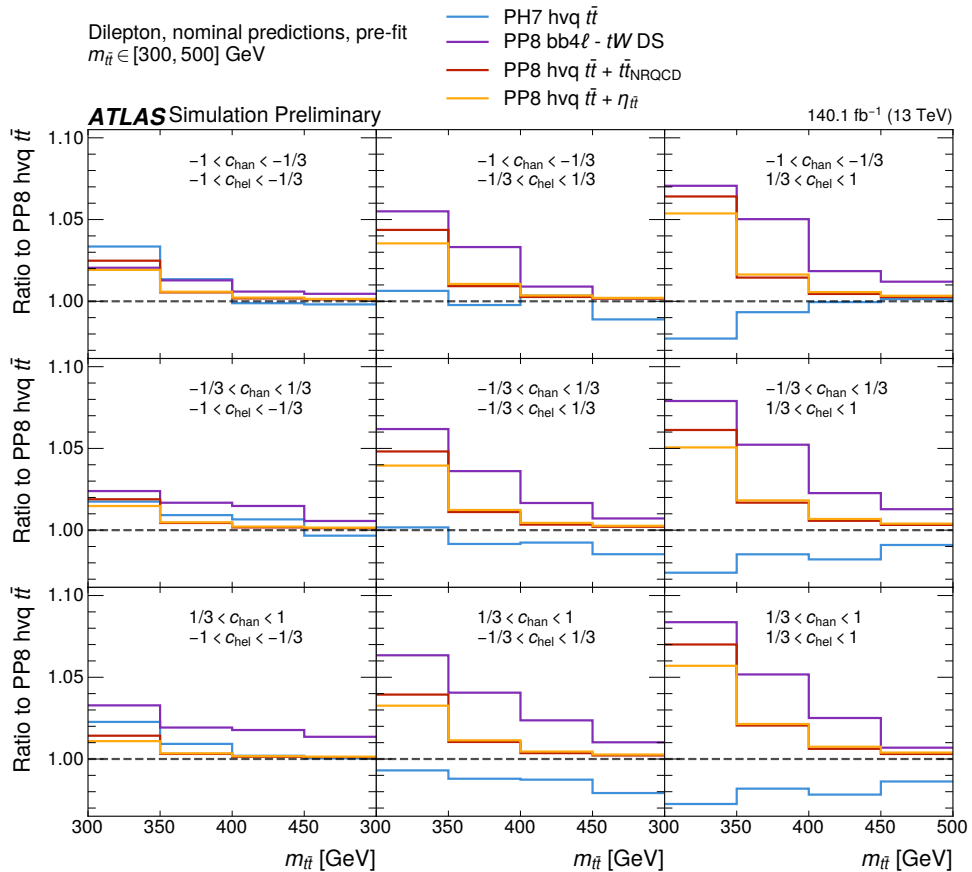


Figure 5: Ratios of the pre-fit distributions of $m_{t\bar{t}}$ in the nine SRs for various $t\bar{t}$ models compared to the baseline Powheg v2 hvq + Pythia 8 prediction. The comparison is made for the extended model with the $t\bar{t}_{\text{NRQCD}}$ prediction and the alternative extended model using the simplified $\eta_{t\bar{t}}$ prediction. In addition, the nominal baseline Powheg v2 hvq + Pythia 8 is compared to two alternative baseline models: one using HERWIG instead of Pythia for the PS and hadronisation and one using Powheg v2 bb41 + Pythia 8 (after the tW contribution is subtracted).

10 Conclusion

A measurement of $t\bar{t}$ production near the kinematic threshold was conducted in events with exactly two leptons, using 140 fb^{-1} of $\sqrt{s} = 13 \text{ TeV}$ pp collision data collected with the ATLAS detector. The invariant-mass distribution of the reconstructed $t\bar{t}$ system was analysed in nine orthogonal signal regions defined based on two angular variables, c_{hel} and c_{han} , evaluated in the $t\bar{t}$ centre-of-mass frame and sensitive to the $t\bar{t}$ spin state including $t\bar{t}_{\text{NRQCD}}$ contributions. The observed data are compared to two model predictions in the range $300 < m_{t\bar{t}} < 500 \text{ GeV}$ using a profile-likehood fit: a baseline model including only pQCD predictions obtained with Powheg v2 hvq + Pythia 8, reweighted to NNLO-QCD+NLO-EW accuracy, and an extended model that includes, in addition, state-of-the-art MC simulations of the formation of a quasi-bound-state enhancement of the cross-section near the $t\bar{t}$ production threshold. The cross-section of the quasi-bound-state contributions is a free parameter in the fit with the extended model. The low $m_{t\bar{t}}$ region is sensitive to effects from off-shell top-quark decays and therefore a systematic uncertainty on the modelling of these effects is included via a comparison between the Powheg v2 hvq + Pythia 8 and an alternative Powheg v2 bb41 + Pythia 8 prediction.

The baseline model Powheg v2 hvq + Pythia 8 without $t\bar{t}$ quasi-bound-state contributions is rejected with an observed (expected) significance of 7.7σ (5.7σ) due to an excess of observed events in the lowest $m_{t\bar{t}}$ bins at large values of the variable c_{hel} . The excess over the Powheg v2 hvq + Pythia 8 prediction corresponds to an observed cross section of $9.0 \pm 1.3 \text{ pb}$.

Further investigations are required to characterise this excess and to better quantify the impact of off-shell top-quark decays and the resummation of higher-order terms in α_s/v close to the threshold that are not included in nominal Powheg v2 hvq + Pythia 8 pQCD prediction but are expected to enhance the cross-section for $t\bar{t}$ production close to threshold [17], compared to the baseline model used here. In this context, extended MC models incorporating additional NRQCD effects, beyond S -wave contributions, such as higher J -states and octet contributions, will also be helpful to investigate the nature of this excess.

Appendix

A Alternative fit with Powheg v2 bb4l + Pythia 8

An alternative model for pQCD $t\bar{t}$ production based on Powheg v2 bb4l + Pythia 8 instead of Powheg v2 hvq + Pythia 8 has also been considered in this analysis. The results obtained with this alternative model for pQCD $t\bar{t}$ production, along with the nominal $t\bar{t}_{\text{NRQCD}}$ model for $t\bar{t}$ quasi-bound-state formation are summarised in the following.

The uncertainties in the Powheg v2 bb4l + Pythia 8 are the same as for the Powheg v2 hvq + Pythia 8 model, with the exception of the uncertainty in the modelling of the top-quark decay and off-shell effects, which is not applicable here. The other uncertainties are derived by taking the relative variations in the Powheg v2 hvq + Pythia 8 model and applying them to the Powheg v2 bb4l + Pythia 8 nominal prediction. The same correlation scheme as for the Powheg v2 hvq + Pythia 8 is used (Section 9).

The $m_{t\bar{t}}$ distributions in the nine SRs before the fit are shown in Figure 6. A deficit in the predicted event yields compared to the data is observed across all SRs and $m_{t\bar{t}}$ bins.

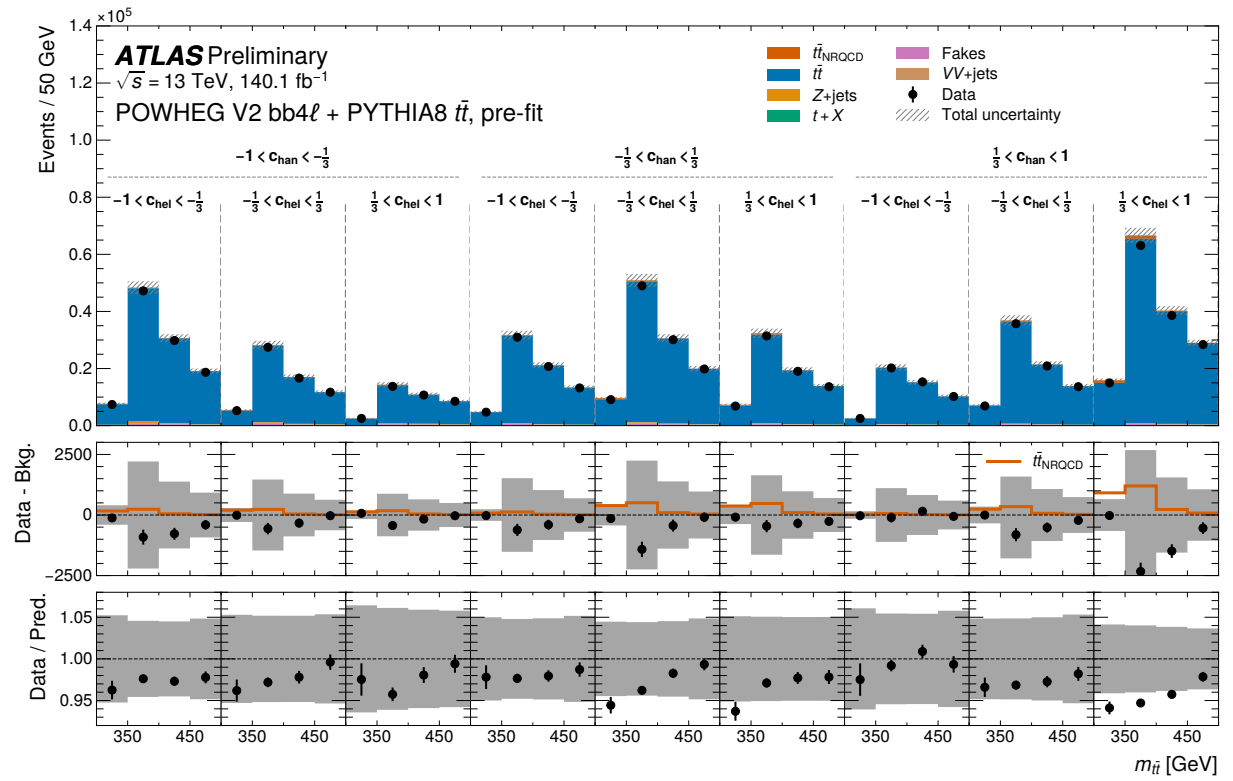


Figure 6: Pre-fit distributions of $m_{t\bar{t}}$ in the nine SRs (upper panel), together with a comparison between the the $t\bar{t}$ quasi-bound-state predictio and the data, from which the pQCD $t\bar{t}$ contribution and background processes have been subtracted (middle panel), and the ratio of the data and the extended $t\bar{t}$ model including $t\bar{t}_{\text{NRQCD}}$ contributions (lower panel) for the Powheg v2 bb4l + Pythia 8 model. The error bars on the data markers represent the statistical uncertainty of the measurement, while the gray hashed and shaded bands represent the total systematic uncertainty in the prediction.

The corresponding distributions after the profile-likelihood fit to data are shown in Figure 7. Good agreement is observed between the data and the predictions of the extended model using Powheg v2 bb41 + Pythia 8 for the pQCD $t\bar{t}$ predictions after the fit. The Goodness-of-Fit is 0.54, compared to a value of 0.057 for the fit with $\mu(t\bar{t}_{\text{NRQCD}}) = 0$. The latter value is larger than the one for the equivalent fit with the Powheg v2 hvq + Pythia 8 baseline model due to the fact that the Powheg v2 bb41 + Pythia 8 model predicts more events at low $m_{t\bar{t}}$ than the Powheg v2 hvq + Pythia 8 model and can thus describe the data in this region better if no quasi-bound-state contribution is included in the fit. The Goodness-of-Fit value for the extended model with Powheg v2 bb41 + Pythia 8 + $t\bar{t}_{\text{NRQCD}}$ is lower than for the nominal fit (Section 9), indicating an overall poorer agreement with the data for this model compared to the nominal Powheg v2 hvq + Pythia 8 + $t\bar{t}_{\text{NRQCD}}$ model.

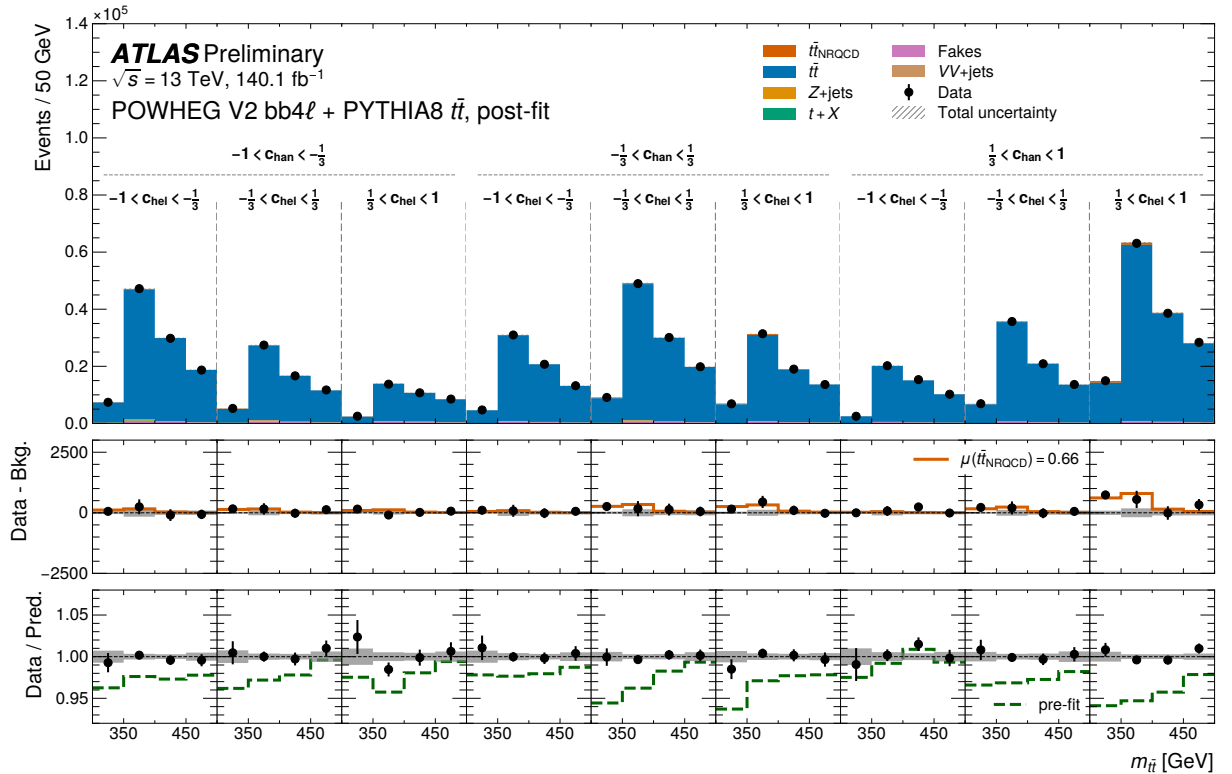


Figure 7: Post-fit distributions of $m_{t\bar{t}}$ in the nine SRs (upper panel), together with a comparison between the $t\bar{t}$ quasi-bound-state prediction and the data, from which the pQCD $t\bar{t}$ contribution and background processes have been subtracted (middle panel), and the ratio of the data and the extended $t\bar{t}$ model including $t\bar{t}_{\text{NRQCD}}$ contributions (lower panel) for the Powheg v2 bb41 + Pythia 8 model. The error bars on the data markers represent the statistical uncertainty of the measurement, while the gray hashed and shaded bands represent the total systematic uncertainty in the prediction.

The cross-section for the $t\bar{t}$ quasi-bound-state sample extracted in the fit to data is

$$\sigma(t\bar{t}_{\text{NRQCD}}) = 4.2 \pm 1.0 = 4.2 \pm 0.8 \text{ (stat.)} \pm 0.5 \text{ (syst.) pb.}$$

This cross-section value is by a factor of 0.7 smaller than the predicted value of 6.43 pb. The null hypothesis $\mu(t\bar{t}_{\text{NRQCD}}) = 0$ is rejected with an observed (expected) significance of 4.3σ (6.3σ). This is consistent with the fact that, while the Powheg v2 bb41 + Pythia 8 model predicts a similar enhancement in $t\bar{t}$ yields at the threshold as quasi-bound-state models compared to Powheg v2 hvq + Pythia 8, it also predicts larger yields at higher values of $m_{t\bar{t}}$ (see the discussion in Section 9), which is disfavoured by the data.

The other normalisation factors extracted from the fit with free-floating $t\bar{t}_{\text{NRQCD}}$ contribution are

$$\begin{aligned}\mu(t\bar{t} + tW) &= 1.00 \pm 0.03 \\ \mu(e\text{-HF-fakes}) &= 1.03 \pm 0.07 \\ \mu(e\text{-PhConv-fakes}) &= 1.01^{+0.15}_{-0.24} \\ \mu(\mu\text{-HF-fakes}) &= 1.16 \pm 0.04 \\ \mu(Z + b) &= 0.45^{+0.30}_{-0.26}.\end{aligned}$$

Their post-fit values are consistent with those obtained in the fit to the model based on Powheg v2 hvq + Pythia 8 (Section 9) within 0.01.

The systematic uncertainties with the largest impact on the extracted $t\bar{t}_{\text{NRQCD}}$ cross-section are shown in Figure 8, and the impact of all uncertainties is summarised in Table 3. Various NPs have been shifted up or down by up to around one pre-fit standard deviation compared to their pre-fit central values, consistent with the poorer pre-fit agreement between the model based on Powheg v2 bb41 + Pythia 8 compared to the model based on Powheg v2 hvq + Pythia 8 (Section 9). The NP related to the recoil-to-top modelling choice is shifted downward by slightly more than a standard deviation, indicating a stronger agreement between the data and the alternative "recoil-to-colour" setting. The NP related to the modelling of FSR in the baseline pQCD $t\bar{t}$ sample is shifted upward by slightly more than a standard deviation. The strongest constraint (0.44) is observed for the correlated component of the PS uncertainty. All other NPs exhibit constraints weaker than 0.5 of their pre-fit standard deviation.

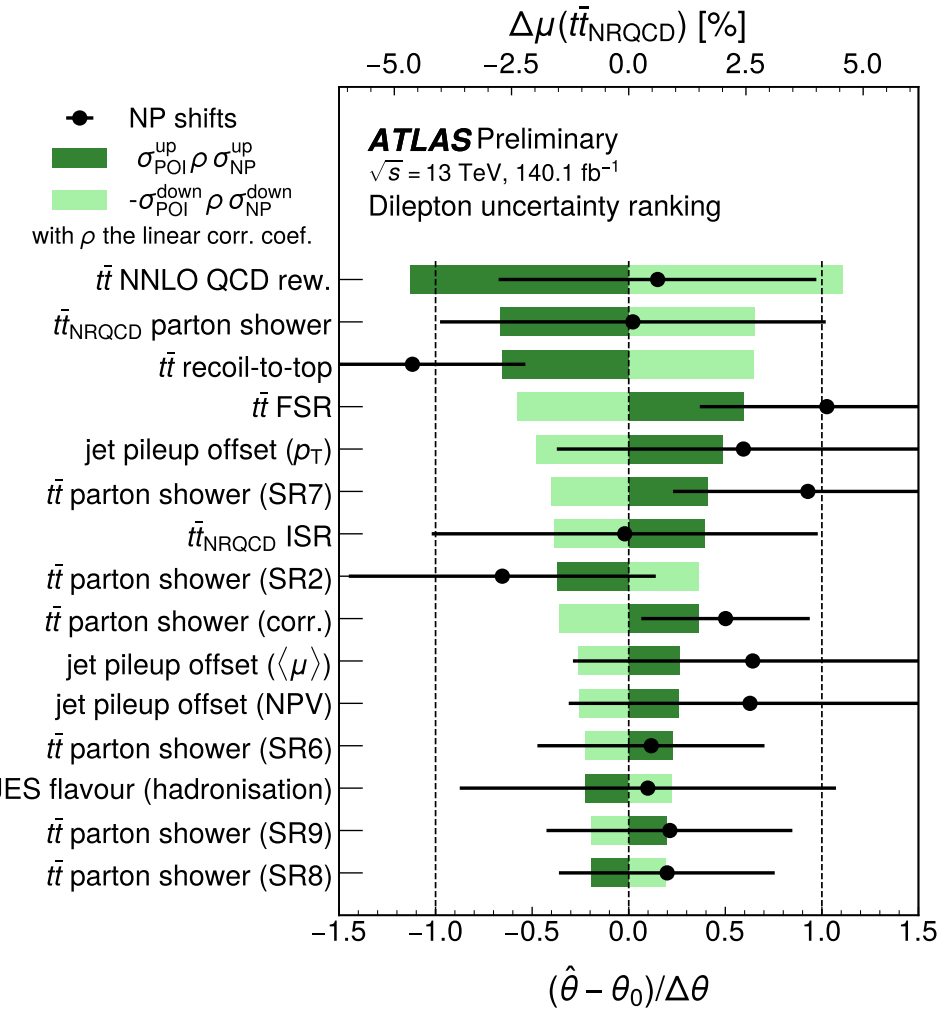


Figure 8: Ranking of the 15 most impactful individual NPs on $\mu(t\bar{t}_{\text{NRQCD}})$ in the profile-likelihood fit with free-floating $\mu(t\bar{t}_{\text{NRQCD}})$. The impact for a given NP is taken as the corresponding off-diagonal element of the fit covariance matrix divided by its pre-fit uncertainty [135] and given in percent on the upper scale. The black marker shows the shifts of the NPs relative to the nominal value θ_0 . They are shown together with their corresponding uncertainty on the lower scale. The SR numbers correspond to the bins introduced in Fig. 1. For the flavour-tagging uncertainties, individual eigenvariations (EVs) are shown.

Table 3: Breakdown of the total uncertainty in the fitted normalisation factor $\mu(t\bar{t}_{\text{NRQCD}})$ into its statistical and systematic components for the model based on PowHEG v2 bb41 + PYTHIA 8. The impact for a given NP is taken as the corresponding off-diagonal element of the fit covariance matrix divided by its pre-fit uncertainty. The impact of a group of NPs is obtained by summing the impacts of all NPs in this category in quadrature. The total systematic uncertainty is obtained by summing in quadrature the impacts of all NPs. The statistical uncertainty in the signal strength is calculated based on the requirement that the sum in quadrature of the statistical uncertainty and the total systematic uncertainty must yield the total uncertainty in the signal strength as obtained from the initial profile likelihood fit in which all nuisance parameters are allowed to float. The category "Instrumental (other)" takes into account the uncertainty in the luminosity, pileup reweighting and jet-vertex tagger efficiency.

Category	Impact
$t\bar{t}$ modelling	10.3%
$t\bar{t}_{\text{NRQCD}}$ modelling	4.8%
Jet energy scale (pileup)	3.9%
Jet energy scale (flavour)	1.4%
Limited MC statistics	1.2%
b -tagging	1.1%
Jet energy resolution	0.9%
Instrumental (other)	0.9%
Jet energy scale (η inter-calibration)	0.8%
Leptons	0.8%
Background normalisations	0.8%
Jet energy scale (other)	0.2%
Total syst. uncertainties	12%
Total stat. uncertainties	20%

B Detailed settings for the Powheg v2 bb4l + Pythia 8 sample

Table 4: Parameter settings used for the Powheg v2 bb4l + Pythia 8 pQCD sample used to define the lineshape uncertainty in the baseline model and as nominal sample for the alternative baseline model documented in App. A.

Parameter	Setting
POWHEG-BOX-RES version	bb4l-beta
PDF (ME)	NNPDF30_NLO
h_{damp}	258.75
Γ_t [GeV]	1.32733
Matching factor between 4FS ME and 5FS PDF	$Q_R = m_b$
ptsqmin	1.44
Inverse-width-correction	yes
Resonance history	$t\bar{t}, tW^-\bar{b}, tW^+b$
PYTHIA version	8.312
PS tune	A14
PDF (PS)	NNPDF2.3LO
POWHEG:veto	1
POWHEG:vetoCount	3
POWHEG:pThard	0
POWHEG:pTemt	0
POWHEG:emitted	0
POWHEG:pTdef	2
POWHEG:nFinal	-1
POWHEG:MPIveto	1
POWHEG:QEDveto	1
POWHEG:bb4l:FSREmission:veto	1
POWHEG:bb4l:vetoQED	0
POWHEG:bb4l:FSREmission:vetoDipoleFrame	0
POWHEG:bb4l:pTpythiaVeto	0
POWHEG:bb4l:ScaleResonance:veto	0
POWHEG:bb4l:pTminVeto	1.2
SpaceShower:pTmaxMatch	2
TimeShower:pTmaxMatch	2
TimeShower:recoilStrategyRF	3 (recoil-to-top)

C Alternative fit with a simplified model of quasi-bound-state effects

The profile-likelihood fit to data used to extract the cross-section for $t\bar{t}$ quasi-bound-state production is performed also with the simplified model described in Section 3.2. This provides a test of the stability of the cross-section estimate and a direct comparison with the results of Ref. [27].

The cross-section for $t\bar{t}$ quasi-bound-state production extracted from the fit with the simplified model is

$$\sigma(\eta_{t\bar{t}}) = 13.4 \pm 1.9 \text{ pb} = 13.4 \pm 1.7 \text{ (stat.)} \pm 1.0 \text{ (syst.) pb.}$$

This is roughly a factor of two larger than the predicted value of 6.43 pb. The null hypothesis $\mu(\eta_{t\bar{t}}) = 0$ is rejected with an observed (expected) significance of 7.8σ (4.0σ). The smaller expected rejection significance compared to the nominal $t\bar{t}_{\text{NRQCD}}$ model is understood to originate from small differences in the $m_{t\bar{t}}$ shape between the two models. As shown in Figure 5, the simplified $\eta_{t\bar{t}}$ model predicts a smaller excess compared to the PowHEG v2 hvq + PYTHIA 8 baseline than the nominal $t\bar{t}_{\text{NRQCD}}$ model in the lowest $m_{t\bar{t}}$ bin but a comparable relative deviation in the second $m_{t\bar{t}}$ bin in each of the SRs. This leads to a smaller expected rejection significance as the relative difference between the extended model with $\eta_{t\bar{t}}$ compared to the baseline PowHEG v2 hvq + PYTHIA 8 model is smaller than for the nominal $t\bar{t}_{\text{NRQCD}}$ model. The larger observed cross-section and rejection significance compared to the nominal $t\bar{t}_{\text{NRQCD}}$ model (Section 9) can also be explained by the differences in the $m_{t\bar{t}}$ distributions in the SRs. To accommodate the excess in the data, which is largest in the lowest $m_{t\bar{t}}$ bins, the post-fit value of the normalisation factor for the simplified model is larger than for the nominal model. The correspondingly larger post-fit yield for the simplified model in the second $m_{t\bar{t}}$ bins is counterbalanced by the fit shifting the much larger PowHEG v2 hvq + PYTHIA 8 background, which exhibits the largest yields in the second $m_{t\bar{t}}$ bins, slightly downward within its systematic uncertainties.

The systematic uncertainties with the largest impact on the extracted cross-section are shown in Figure 9. Downward shifts are observed for the nuisance parameter related to the modelling of the top-quark decay and off-shell effects. Overall, the relative impacts and constraints are largely comparable with those obtained in the main fit. The impact of all uncertainties is summarised in Table 5.

The other normalisation factors extracted from the fit with free-floating $\eta_{t\bar{t}}$ contribution are

$$\begin{aligned}\mu(t\bar{t}) &= 0.98 \pm 0.03 \\ \mu(e\text{-HF-fakes}) &= 1.03 \pm 0.07 \\ \mu(e\text{-PhConv-fakes}) &= 1.03^{+0.15}_{-0.23} \\ \mu(\mu\text{-HF-fakes}) &= 1.18 \pm 0.04 \\ \mu(Z + b) &= 0.68^{+0.38}_{-0.32}.\end{aligned}$$

The $m_{t\bar{t}}$ distributions in the nine SRs before and after this fit are shown in Figures 10 and 11, respectively. Good agreement is observed between the data and the predictions based on PowHEG v2 hvq + PYTHIA 8 and the simplified model for quasi-bound-state production, with a Goodness-of-Fit value of 0.95. As for the main result presented in the paper body, the contribution of quasi-bound-state effects is largest in the bin with $\frac{1}{3} < c_{\text{hel}} < 1$, $\frac{1}{3} < c_{\text{han}} < 1$ and at low values of $m_{t\bar{t}}$.

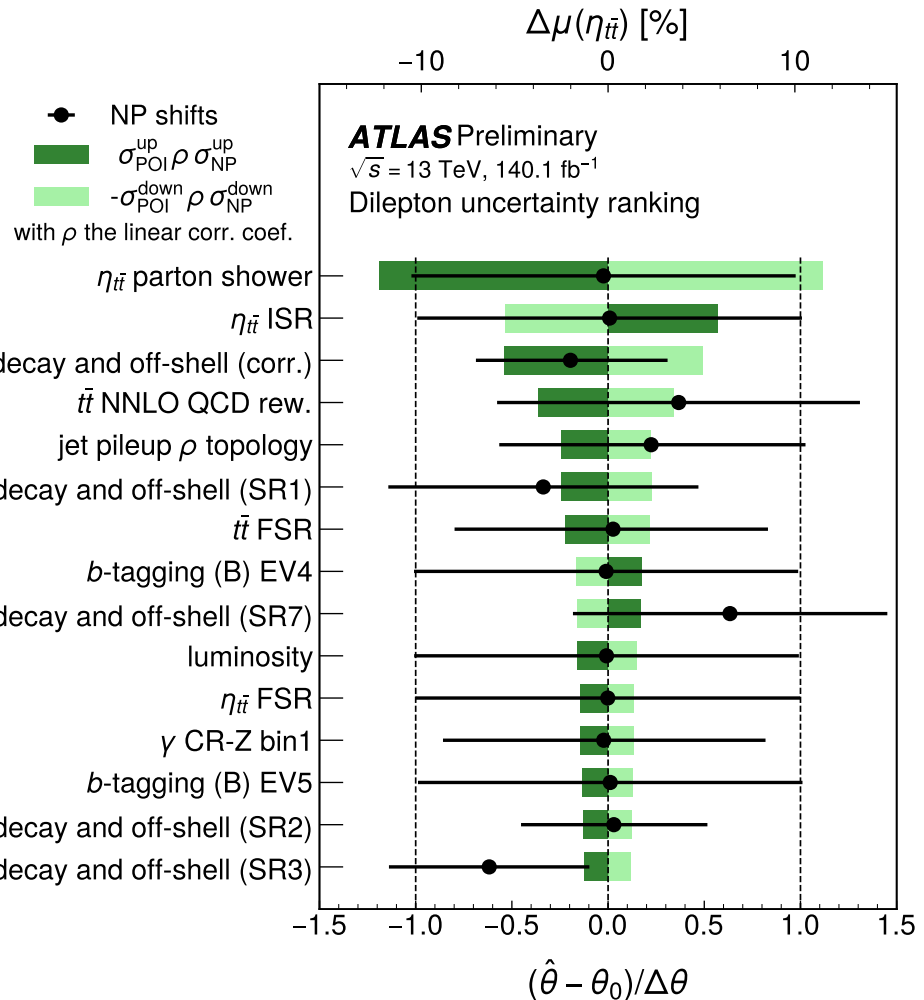


Figure 9: Ranking of the 15 most impactful individual NPs on $\mu(\eta_{t\bar{t}})$ in the profile-likelihood fit when using the simplified model of $\eta_{t\bar{t}}$. The impact for a given NP is taken as the corresponding off-shell element of the fit covariance matrix divided by the pre-fit uncertainty [135] and given in percent on the upper scale. The black marker shows the shifts of the NPs relative to the nominal value θ_0 . They are shown together with their corresponding uncertainties on the lower scale. The SR numbers correspond to the bins introduced in Fig. 1. For the flavour-tagging uncertainties, individual eigenvariations (EVs) are shown.

Table 5: Breakdown of the total uncertainty in the fitted normalisation factor $\mu(\eta_{t\bar{t}})$ into its statistical and systematic components. The impact for a given NP is taken as the corresponding off-diagonal element of the fit covariance matrix divided by its pre-fit uncertainty. The impact of a group of NPs is obtained by summing the impacts of all NPs in this category in quadrature. The total systematic uncertainty is obtained by summing in quadrature the impacts of all NPs. The statistical uncertainty in the signal strength is calculated based on the requirement that the sum in quadrature of the statistical uncertainty and the total systematic uncertainty must yield the total uncertainty in the signal strength as obtained from the initial profile likelihood fit in which all nuisance parameters are allowed to float. The category "Instrumental (other)" takes into account the uncertainty in the luminosity, pileup reweighting and jet-vertex tagger efficiency.

Category	Impact
$\eta_{t\bar{t}}$ modelling	6.3%
$t\bar{t}$ modelling	3.9%
b -tagging	1.2%
Jet energy scale (pileup)	1.2%
Instrumental (other)	0.9%
Limited MC statistics	0.7%
Jet energy scale (flavour)	0.5%
Background normalisations	0.4%
Jet energy scale (η inter-calibration)	0.4%
tW modelling	0.4%
Jet energy scale (other)	0.4%
Jet energy resolution	0.3%
Leptons	0.3%
Total syst. uncertainties	7.7%
Total stat. uncertainties	12%

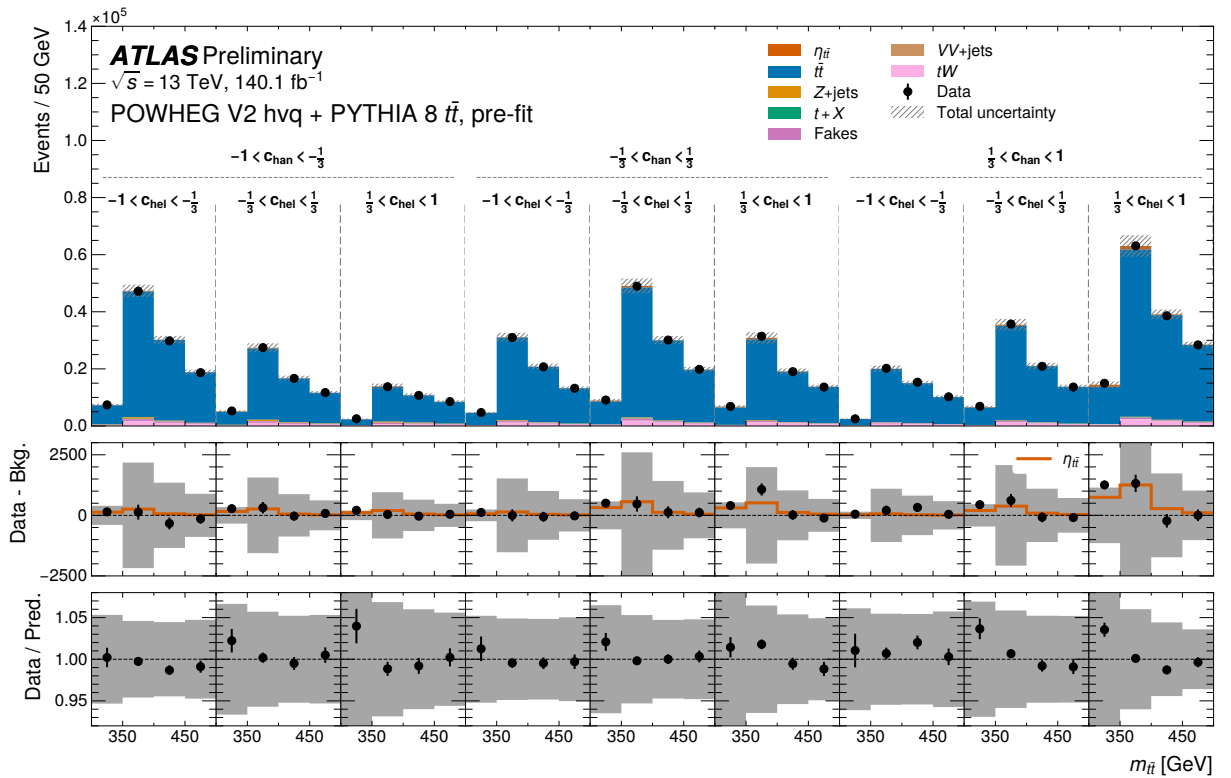


Figure 10: Pre-fit distributions of $m_{t\bar{t}}$ in the nine SRs (upper panel), together with a comparison between the $t\bar{t}$ quasi-bound-state prediction, based on the simplified $\eta_{t\bar{t}}$ model, and the data, from which the pQCD $t\bar{t}$ contribution and background processes have been subtracted (middle panel), and the ratio of the data and the extended $t\bar{t}$ model including $\eta_{t\bar{t}}$ contributions (lower panel). The error bars on the data markers represent the statistical uncertainty of the measurement, while the gray hashed and shaded bands represent the total systematic uncertainty in the prediction.

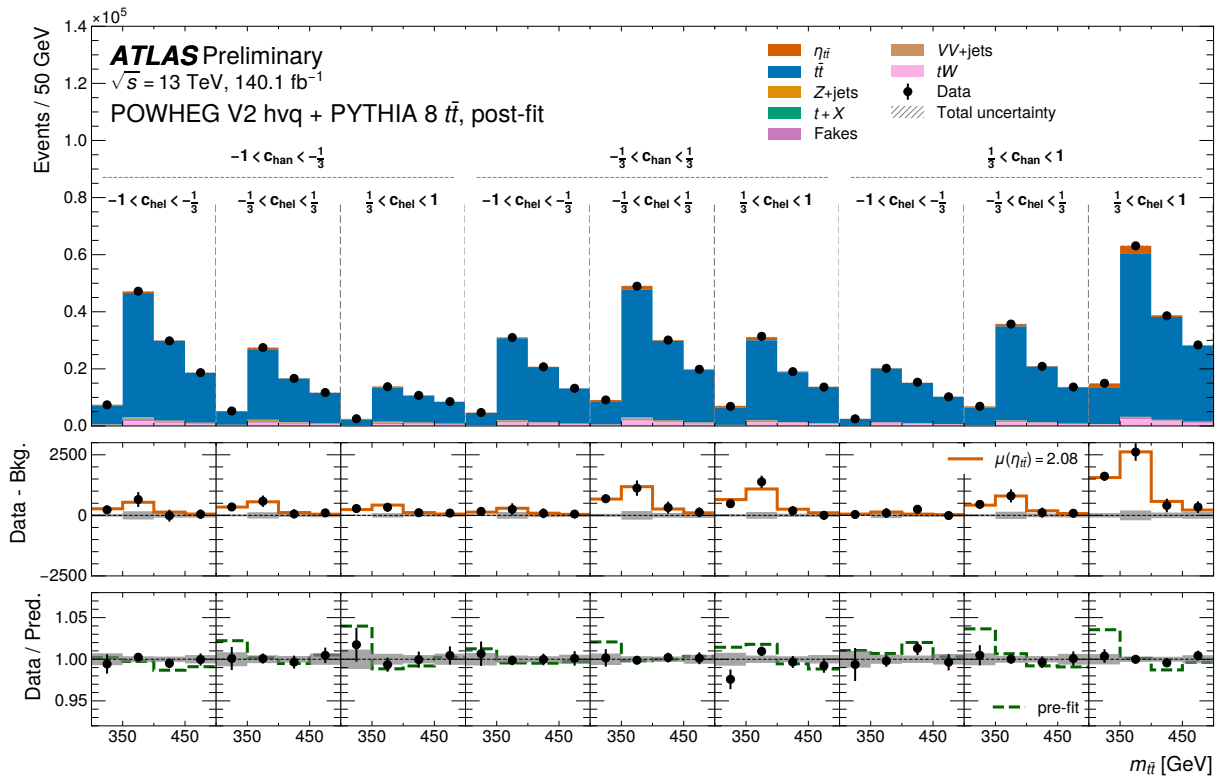


Figure 11: Post-fit distributions in the nine SRs (upper panel), together with a comparison between the $t\bar{t}$ quasi-bound-state prediction, based on the simplified $\eta_{t\bar{t}}$ model, and the data, from which the pQCD $t\bar{t}$ contribution and background processes have been subtracted (middle panel), and the ratio of the data to the extended $t\bar{t}$ model including $\eta_{t\bar{t}}$ contributions (lower panel). The error bars on the data markers represent the statistical uncertainty of the measurement, while the gray hashed and shaded bands represent the total systematic uncertainty in the prediction.

D Post-fit distributions for the control regions

The post-fit distributions of the trailing lepton p_T in the CR-Fakes regions and $m_{t\bar{t}}$ in the CR-Z region are shown in Figure 12. Good agreement between the data and the predictions is observed in all distributions.

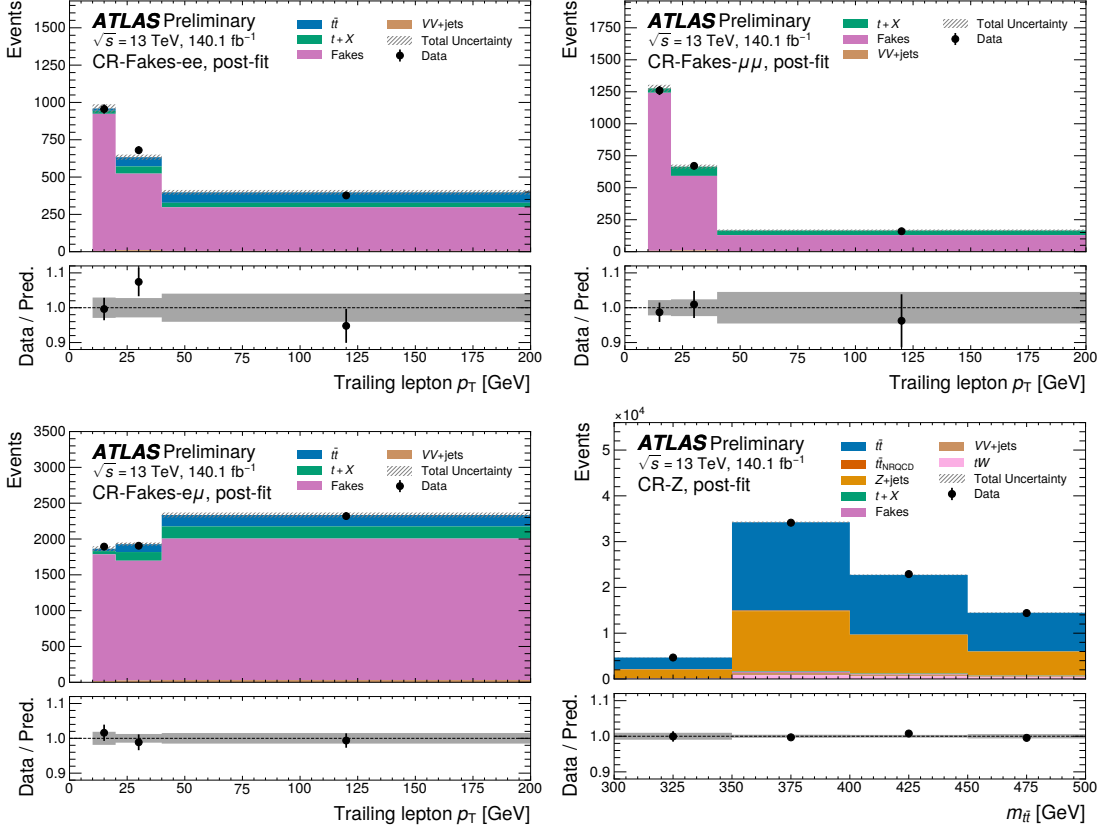


Figure 12: Post-fit distributions in the four control regions: the trailing lepton p_T in the CR-Fakes regions for the ee (top left), $\mu\mu$ (top right), and $e\mu$ (bottom left) channels, and $m_{t\bar{t}}$ in CR-Z (bottom right). The error bars on the data markers represent the statistical uncertainty of the measurement, while the hashed and shaded bands represent the total systematic uncertainty in the SM predictions.

E Pre-fit yields in the signal and control regions

Table 6: Observed and expected yields in the signal and control regions before the profile-likelihood fit to data. The $t\bar{t}$ expected yields are provided for the baseline PowHEG v2 $h\nu q + \text{PyTHIA 8}$ sample, as well as for the PowHEG v2 bb41 + PyTHIA 8 sample, which includes contributions from both $t\bar{t}$ and tW . The expected yields for the quasi-bound-state samples are given for the nominal quasi-bound-state model ($t\bar{t}_{\text{NRQCD}}$) and for the simplified model ($\eta_{t\bar{t}}$). The total expected yields are calculated for the baseline samples used in the analysis, and for the alternative PowHEG v2 bb41 + PyTHIA 8 sample, and include the contribution of $t\bar{t}_{\text{NRQCD}}$. The quoted uncertainties include all sources of systematic uncertainty. Since the rounding is applied to the individual values, the total uncertainty does not always reflect the sum in quadrature of the individual components.

	SR1	SR2	SR3	SR4	SR5	SR6	SR7	SR8	SR9
$t\bar{t}$	97000 ± 4000	55600 ± 3100	31500 ± 2100	65100 ± 3200	100000 ± 5000	65000 ± 4000	44500 ± 2500	72000 ± 4000	135000 ± 7000
tW	3650 ± 240	2430 ± 180	1620 ± 140	2590 ± 180	4060 ± 280	2930 ± 240	1870 ± 160	2840 ± 190	5400 ± 400
$t\bar{t} + W$ (bb41)	102000 ± 5000	59600 ± 3100	34000 ± 2100	68900 ± 3300	108000 ± 5000	70000 ± 4000	47100 ± 2600	77000 ± 4000	147000 ± 6000
$t\bar{t}_{\text{NRQCD}}$	476 ± 26	489 ± 27	374 ± 20	255 ± 13	1030 ± 50	990 ± 40	121 ± 6	685 ± 31	2430 ± 90
$\eta_{t\bar{t}}$	476 ± 21	503 ± 24	392 ± 20	264 ± 11	1060 ± 40	990 ± 40	128 ± 6	704 ± 28	2380 ± 90
Z+jets	990 ± 140	880 ± 130	870 ± 110	490 ± 80	680 ± 90	520 ± 90	230 ± 50	350 ± 50	540 ± 90
$t + X$	320 ± 100	180 ± 50	105 ± 32	200 ± 60	280 ± 80	170 ± 50	140 ± 40	190 ± 60	310 ± 90
Fakes	1480 ± 50	1200 ± 40	1020 ± 40	1090 ± 40	1430 ± 60	996 ± 34	803 ± 27	950 ± 60	1127 ± 33
VV+jets	120 ± 40	104 ± 32	92 ± 29	79 ± 25	120 ± 40	104 ± 32	54 ± 17	80 ± 25	140 ± 40
Total	104000 ± 5000	60900 ± 3300	35600 ± 2200	69800 ± 3400	108000 ± 5000	71000 ± 4000	47800 ± 2600	77000 ± 4000	145000 ± 7000
Total (bb41)	106000 ± 5000	62500 ± 3200	36500 ± 2200	71100 ± 3400	111000 ± 5000	73000 ± 4000	48400 ± 2600	79000 ± 4000	152000 ± 6000
Data	103095	61071	35514	69602	107995	70917	48258	77123	145030
	CR-Z	CR-Fakes- $e\mu$	CR-Fakes- ee	CR-Fakes- $\mu\mu$					
$t\bar{t}$	43500 ± 2000	460 ± 230	220 ± 110	—	—	—	—	—	—
tW	1830 ± 130	—	—	—	—	—	—	—	—
$t\bar{t} + W$ (bb41)	46000 ± 2000	480 ± 240	240 ± 120	< 0.1	< 0.1	< 0.1	< 0.1	< 0.1	< 0.1
$t\bar{t}_{\text{NRQCD}}$	204 ± 12	—	—	—	—	—	—	—	—
$\eta_{t\bar{t}}$	237 ± 11	< 0.1	< 0.1	< 0.1	< 0.1	< 0.1	< 0.1	< 0.1	< 0.1
Z+jets	33000 ± 6000	—	—	—	—	—	—	—	—
$t + X$	330 ± 100	370 ± 110	109 ± 33	—	—	—	—	—	—
Fakes	484 ± 23	4890 ± 130	1640 ± 70	1650 ± 60	1650 ± 60	1650 ± 60	1650 ± 60	1650 ± 60	1650 ± 60
VV+jets	1100 ± 350	110 ± 60	30 ± 15	30 ± 15	30 ± 15	30 ± 15	30 ± 15	30 ± 15	30 ± 15
Total	80000 ± 7000	5830 ± 340	2000 ± 160	1840 ± 80	1840 ± 80	1840 ± 80	1840 ± 80	1840 ± 80	1840 ± 80
Total (bb41)	81000 ± 7000	5850 ± 350	2020 ± 170	1840 ± 80	1840 ± 80	1840 ± 80	1840 ± 80	1840 ± 80	1840 ± 80
Data	76127	6120	2013	2091	2091	2091	2091	2091	2091

F Comparison of the different $t\bar{t}$ models in bins of c_{hel} and c_{han}

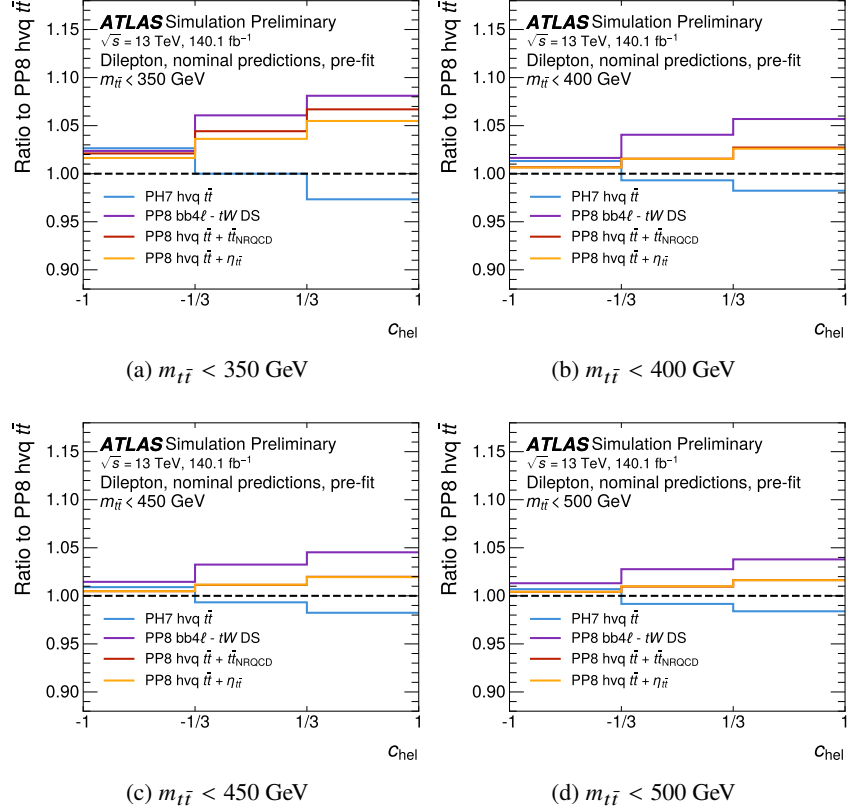


Figure 13: Ratios of the pre-fit distributions of c_{hel} for various $t\bar{t}$ MC models compared to the baseline PowHEG v2 + PYTHIA 8 prediction. The comparison is made for the extended model with the $t\bar{t}_{\text{NRQCD}}$ prediction and the alternative extended model using the simplified $\eta_{t\bar{t}}$ prediction. In addition, the nominal baseline PowHEG v2 hvq + PYTHIA 8 is compared to two alternative baseline models: one using HERWIG 7 instead of PYTHIA 8 for the PS and hadronisation and one using PowHEG v2 bb4f + PYTHIA 8 (subtracting the tW contribution). The ratios are evaluated for different upper limits on $m_{t\bar{t}}$: (a) $m_{t\bar{t}} < 350$ GeV, (b) $m_{t\bar{t}} < 400$ GeV, (c) $m_{t\bar{t}} < 450$ GeV, (d) $m_{t\bar{t}} < 500$ GeV.

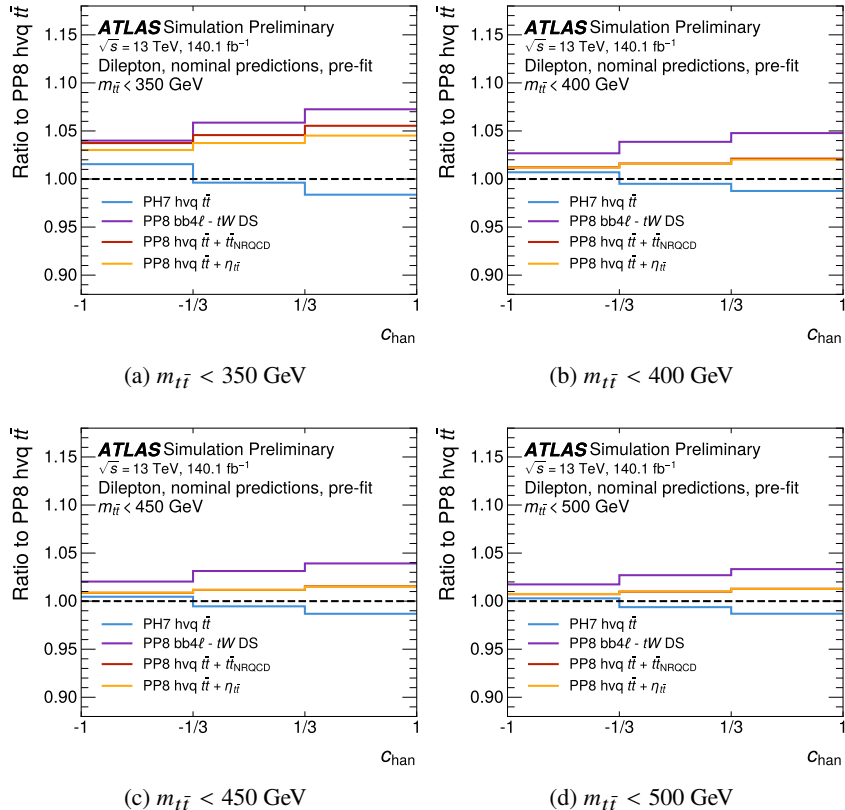


Figure 14: Ratios of the pre-fit distributions of c_{han} for various $t\bar{t}$ MC models compared to the baseline PowHEG v2 hvq + PYTHIA 8 prediction. The comparison is made for the extended model with the $t\bar{t}_{\text{NRQCD}}$ prediction and the alternative extended model using the simplified $\eta_{t\bar{t}}$ prediction. In addition, the nominal baseline PowHEG v2 hvq + PYTHIA 8 is compared to two alternative baseline models: one using HERWIG 7 instead of PYTHIA 8 for the PS and hadronisation and one using PowHEG v2 bb4l + PYTHIA 8 (subtracting the tW contribution). The ratios are evaluated for different upper limits on $m_{t\bar{t}}$: (a) $m_{t\bar{t}} < 350$ GeV, (b) $m_{t\bar{t}} < 400$ GeV, (c) $m_{t\bar{t}} < 450$ GeV, (d) $m_{t\bar{t}} < 500$ GeV.

G Event display

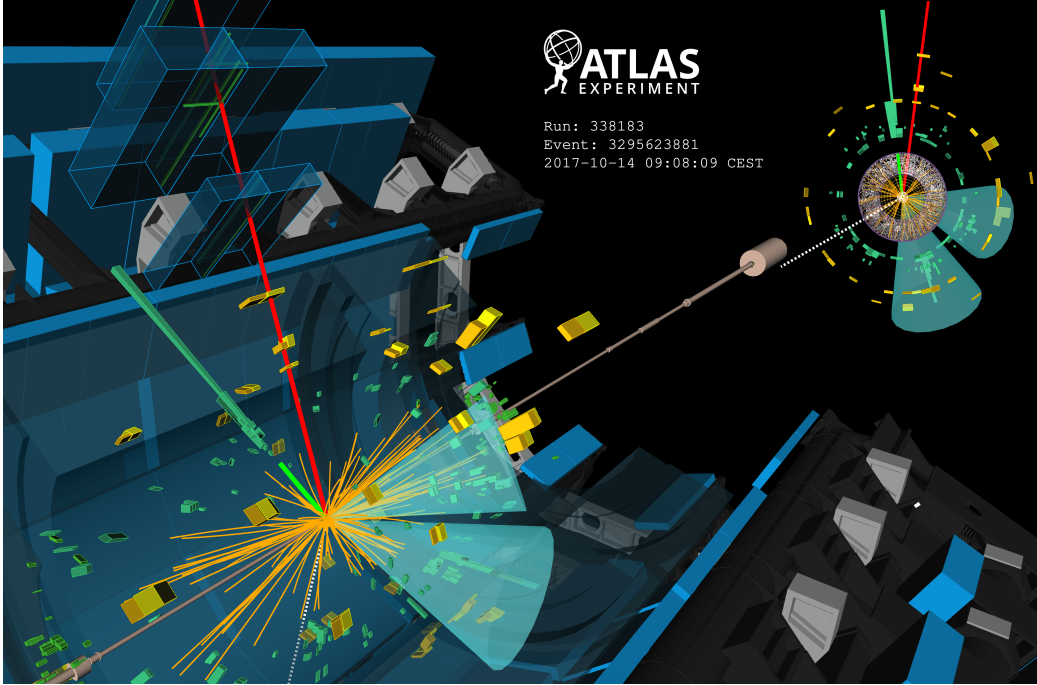


Figure 15: Event display of a candidate event consistent with the formation of a $t\bar{t}$ quasi-bound-state. The event (Run number 338183 Event number 3295623881, recorded on October 14, 2017) is selected based on properties of the $t\bar{t}$ pair. In particular, the invariant mass of the $t\bar{t}$ pair in the event is 342 GeV, and the values of the spin-sensitive observables c_{hel} and c_{han} are 0.97 and 0.94, respectively. The mass of the top (antitop) in the event is 167 GeV (172 GeV), and the magnitude of the top momentum in the top-quark pair rest frame, p^* , is 25 GeV. In this 3D cut-away view of the ATLAS detector, several radial sectors have been removed to expose the interior. In this event, each top quark decays into a b quark and a W boson. The two W bosons then decay leptonically: one into an electron (green line) and an electron neutrino, and the other into a muon (red line) and a muon neutrino. The neutrinos are represented by the missing energy in the event, shown as the dashed white line. The event contains two jets from the b -quarks, shown as turquoise cones. Tracks of charged particles reconstructed in the inner detector, and with transverse momentum greater than 1 GeV, are visualised as orange lines. Green/teal rectangles correspond to energy deposits in cells of the electromagnetic calorimeter, while yellow/orange rectangles correspond to energy deposits in cells of the hadron calorimeter. Muon chambers in the barrel region are shown as semi-transparent blue boxes; inside them, the measurements associated with the muon are shown as green lines. The top-right inlay presents a transverse-plane projection of the same event, showing the electron (green line) and muon (red line) tracks and the direction of the b -tagged jets (turquoise cones) and missing energy (dashed white line). Starting from the center, the radial view shows the hits in the Pixel (white dots), SCT (yellow), and TRT (white/red) detectors.

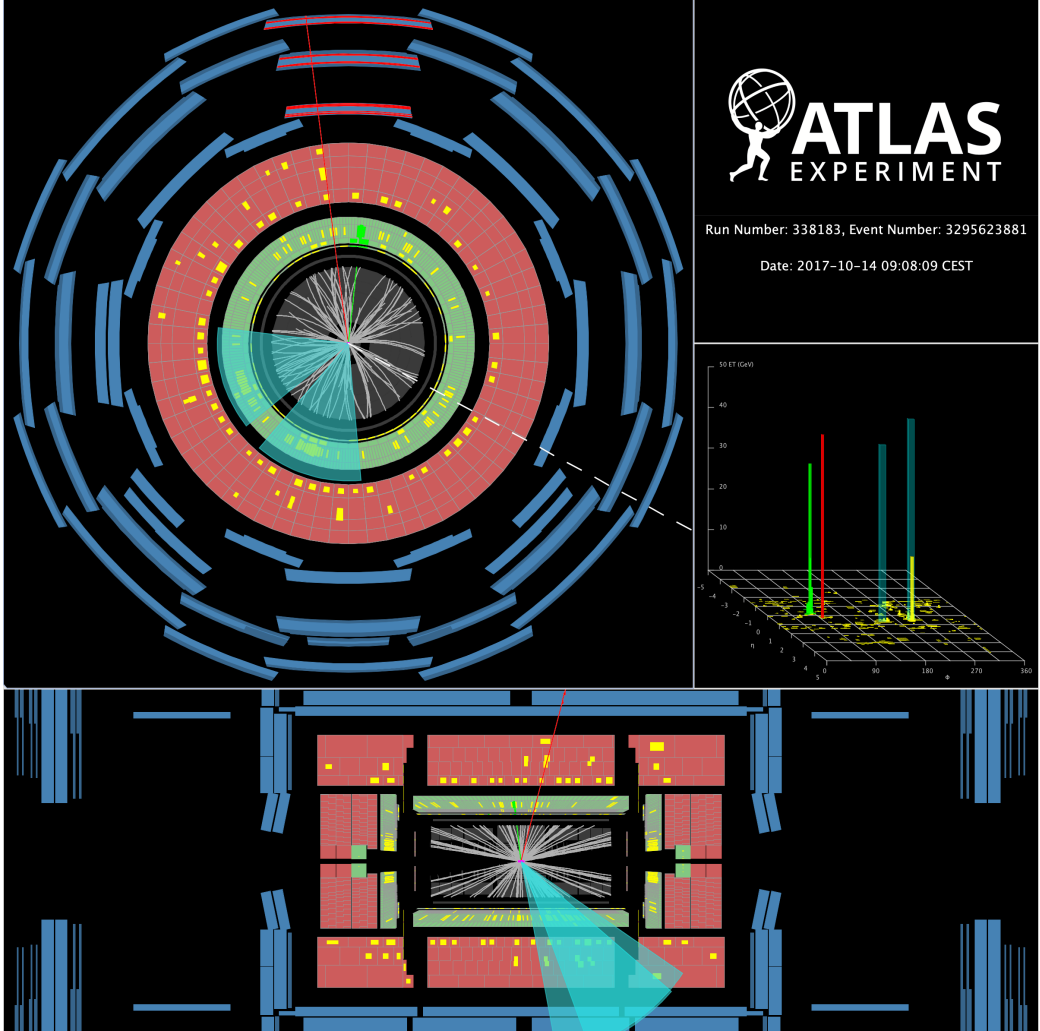


Figure 16: Event display of a candidate event consistent with the formation of a $t\bar{t}$ quasi-bound-state (Run number 338183 Event number 3295623881, recorded on October 14, 2017). The invariant mass of the $t\bar{t}$ pair in the event is 342.2 GeV. The values of the spin-sensitive observables c_{hel} and c_{han} are 0.965 and 0.944, respectively. The candidate event is reconstructed in the $bb\mu e$ final state. The image features two views of the same event: a transversal view of the ATLAS detector on the top and a longitudinal view on the bottom. The red line shows the path of the muon, including the hits in the muon spectrometer. The green line shows the path of the electron together with its energy deposits in the electromagnetic calorimeter. The turquoise cones are the two b-tagged jets. As shown in the "lego plot" on the right, the muon and electron candidates have transverse momenta of 45 GeV and 37 GeV, respectively. The two jets have transverse momenta of 49 GeV and 43 GeV. The event misses a transverse momentum of about 99 GeV.

References

- [1] Y. Kiyo, J. H. Kuhn, S. Moch, M. Steinhauser and P. Uwer, *Top-quark pair production near threshold at LHC*, *Eur. Phys. J. C* **60** (2009) 375, arXiv: [0812.0919 \[hep-ph\]](#) (cit. on pp. 2, 6, 7).
- [2] Y. Afik and J. R. M. de Nova, *Entanglement and quantum tomography with top quarks at the LHC*, *Eur. Phys. J. Plus* **136** (2021) 907, arXiv: [2003.02280 \[quant-ph\]](#) (cit. on pp. 2, 10).
- [3] ATLAS Collaboration, *Observation of quantum entanglement with top quarks at the ATLAS detector*, *Nature* **633** (2024) 542, arXiv: [2311.07288 \[hep-ex\]](#) (cit. on pp. 2, 10).
- [4] CMS Collaboration, *Observation of quantum entanglement in top quark pair production in proton–proton collisions at $\sqrt{s} = 13$ TeV*, *Rept. Prog. Phys.* **87** (2024) 117801, arXiv: [2406.03976 \[hep-ex\]](#) (cit. on pp. 2, 3, 7, 10).
- [5] CMS Collaboration, *Measurement of the top quark Yukawa coupling from $t\bar{t}$ kinematic distributions in the lepton+jets final state in proton–proton collisions at $\sqrt{s} = 13$ TeV*, *Phys. Rev. D* **100** (2019) 072007, arXiv: [1907.01590 \[hep-ex\]](#) (cit. on p. 2).
- [6] I. I. Y. Bigi, Y. L. Dokshitzer, V. A. Khoze, J. H. Kuhn and P. M. Zerwas, *Production and Decay Properties of Ultraheavy Quarks*, *Phys. Lett. B* **181** (1986) 157 (cit. on p. 2).
- [7] V. S. Fadin and V. A. Khoze, *Threshold Behavior of Heavy Top Production in e^+e^- Collisions*, *JETP Lett.* **46** (1987) 525 (cit. on p. 2).
- [8] V. S. Fadin, V. A. Khoze and T. Sjostrand, *On the Threshold Behavior of Heavy Top Production*, *Z. Phys. C* **48** (1990) 613 (cit. on pp. 2, 7).
- [9] Y. Sumino, K. Fujii, K. Hagiwara, H. Murayama and C. K. Ng, *Top quark pair production near threshold*, *Phys. Rev. D* **47** (1993) 56 (cit. on p. 2).
- [10] S. Abachi et al., *Observation of the top quark*, *Phys. Rev. Lett.* **74** (1995) 2632, arXiv: [hep-ex/9503003](#) (cit. on p. 2).
- [11] F. Abe et al., *Observation of top quark production in $\bar{p}p$ collisions*, *Phys. Rev. Lett.* **74** (1995) 2626, arXiv: [hep-ex/9503002](#) (cit. on p. 2).
- [12] W. E. Caswell and G. P. Lepage, *Effective Lagrangians for Bound State Problems in QED, QCD, and Other Field Theories*, *Phys. Lett. B* **167** (1986) 437 (cit. on p. 2).
- [13] G. T. Bodwin, E. Braaten and G. P. Lepage, *Rigorous QCD analysis of inclusive annihilation and production of heavy quarkonium*, *Phys. Rev. D* **51** (1995) 1125, [Erratum: Phys.Rev.D 55, 5853 (1997)], arXiv: [hep-ph/9407339](#) (cit. on p. 2).
- [14] K. Hagiwara, Y. Sumino and H. Yokoya, *Bound-state Effects on Top Quark Production at Hadron Colliders*, *Phys. Lett. B* **666** (2008) 71, arXiv: [0804.1014 \[hep-ph\]](#) (cit. on p. 2).
- [15] Y. Sumino and H. Yokoya, *Bound-state effects on kinematical distributions of top quarks at hadron colliders*, *JHEP* **09** (2010) 034, [Erratum: JHEP 06, 037 (2016)], arXiv: [1007.0075 \[hep-ph\]](#) (cit. on pp. 2, 7).

- [16] M. V. Garzelli, G. Limatola, S.-O. Moch, M. Steinhauser and O. Zenaiev, *Updated predictions for toponium production at the LHC*, (2024), arXiv: [2412.16685 \[hep-ph\]](#) (cit. on p. 2).
- [17] P. Nason, E. Re and L. Rottoli, *Spin Correlations in $t\bar{t}$ Production and Decay at the LHC in QCD Perturbation Theory*, (2025), arXiv: [2505.00096 \[hep-ph\]](#) (cit. on pp. 2, 23).
- [18] W.-L. Ju et al., *Top quark pair production near threshold: single/double distributions and mass determination*, *JHEP* **06** (2020) 158, arXiv: [2004.03088 \[hep-ph\]](#) (cit. on p. 2).
- [19] T. Ježo, J. M. Lindert, P. Nason, C. Oleari and S. Pozzorini, *An NLO+PS generator for $t\bar{t}$ and Wt production and decay including non-resonant and interference effects*, *Eur. Phys. J. C* **76** (2016) 691, arXiv: [1607.04538 \[hep-ph\]](#) (cit. on pp. 2, 6).
- [20] T. Ježo, J. M. Lindert and S. Pozzorini, *Resonance-aware NLOPS matching for off-shell $t\bar{t} + tW$ production with semileptonic decays*, *JHEP* **10** (2023) 008, arXiv: [2307.15653 \[hep-ph\]](#) (cit. on pp. 2, 6).
- [21] ATLAS Collaboration, *Measurement of the $t\bar{t}$ production cross-section and lepton differential distributions in $e\mu$ dilepton events from pp collisions at $\sqrt{s} = 13$ TeV with the ATLAS detector*, *Eur. Phys. J. C* **80** (2020) 528, arXiv: [1910.08819 \[hep-ex\]](#) (cit. on p. 2).
- [22] ATLAS Collaboration, *Inclusive and differential cross-sections for dilepton $t\bar{t}$ production measured in $\sqrt{s} = 13$ TeV pp collisions with the ATLAS detector*, *JHEP* **07** (2023) 141, arXiv: [2303.15340 \[hep-ex\]](#) (cit. on p. 2).
- [23] CMS Collaboration, *Differential cross section measurements for the production of top quark pairs and of additional jets using dilepton events from pp collisions at $\sqrt{s} = 13$ TeV*, *JHEP* **02** (2025) 064, arXiv: [2402.08486 \[hep-ex\]](#) (cit. on p. 2).
- [24] CMS Collaboration, *Measurements of polarization and spin correlation and observation of entanglement in top quark pairs using lepton+jets events from proton–proton collisions at $\sqrt{s} = 13$ TeV*, *Phys. Rev. D* **110** (2024) 112016, arXiv: [2409.11067 \[hep-ex\]](#) (cit. on pp. 3, 7).
- [25] B. Fuks, K. Hagiwara, K. Ma and Y.-J. Zheng, *Signatures of toponium formation in LHC run 2 data*, *Phys. Rev. D* **104** (2021) 034023, arXiv: [2102.11281 \[hep-ph\]](#) (cit. on pp. 3, 6, 7, 21).
- [26] F. Maltoni, C. Severi, S. Tentori and E. Vryonidou, *Quantum detection of new physics in top-quark pair production at the LHC*, *JHEP* **03** (2024) 099, arXiv: [2401.08751 \[hep-ph\]](#) (cit. on pp. 3, 7, 21).
- [27] CMS Collaboration, *Observation of a pseudoscalar excess at the top quark pair production threshold*, (2025), arXiv: [2503.22382 \[hep-ex\]](#) (cit. on pp. 3, 7, 30).
- [28] B. Fuks, K. Hagiwara, K. Ma and Y.-J. Zheng, *Simulating toponium formation signals at the LHC*, *Eur. Phys. J. C* **85** (2025) 157, arXiv: [2411.18962 \[hep-ph\]](#) (cit. on pp. 3, 6, 7).
- [29] B. Fuks, ‘Toponium physics at the Large Hadron Collider’, *59th Rencontres de Moriond on Electroweak Interactions and Unified Theories*, 2025, arXiv: [2505.03869 \[hep-ph\]](#) (cit. on pp. 3, 7).

- [30] ATLAS Collaboration, *The ATLAS Experiment at the CERN Large Hadron Collider*, JINST **3** (2008) S08003 (cit. on p. 3).
- [31] G. Avoni et al., *The new LUCID-2 detector for luminosity measurement and monitoring in ATLAS*, JINST **13** (2018) P07017 (cit. on p. 4).
- [32] ATLAS Collaboration, *Performance of the ATLAS trigger system in 2015*, Eur. Phys. J. C **77** (2017) 317, arXiv: [1611.09661 \[hep-ex\]](#) (cit. on p. 4).
- [33] ATLAS Collaboration, *Software and computing for Run 3 of the ATLAS experiment at the LHC*, Eur. Phys. J. C **85** (2025) 234, arXiv: [2404.06335 \[hep-ex\]](#) (cit. on p. 4).
- [34] ATLAS Collaboration, *Luminosity determination in pp collisions at $\sqrt{s} = 13$ TeV using the ATLAS detector at the LHC*, Eur. Phys. J. C **83** (2023) 982, arXiv: [2212.09379 \[hep-ex\]](#) (cit. on pp. 4, 13).
- [35] ATLAS Collaboration, *Performance of the ATLAS muon triggers in Run 2*, JINST **15** (2020) P09015, arXiv: [2004.13447 \[physics.ins-det\]](#) (cit. on p. 4).
- [36] ATLAS Collaboration, *Performance of electron and photon triggers in ATLAS during LHC Run 2*, Eur. Phys. J. C **80** (2020) 47, arXiv: [1909.00761 \[hep-ex\]](#) (cit. on p. 4).
- [37] ATLAS Collaboration, *The ATLAS Simulation Infrastructure*, Eur. Phys. J. C **70** (2010) 823, arXiv: [1005.4568 \[physics.ins-det\]](#) (cit. on p. 4).
- [38] S. Agostinelli et al., *GEANT4 – a simulation toolkit*, Nucl. Instrum. Meth. A **506** (2003) 250 (cit. on p. 4).
- [39] ATLAS Collaboration, *The simulation principle and performance of the ATLAS fast calorimeter simulation FastCaloSim*, ATL-PHYS-PUB-2010-013, 2010, URL: <https://cds.cern.ch/record/1300517> (cit. on p. 4).
- [40] T. Sjöstrand, S. Mrenna and P. Skands, *A brief introduction to PYTHIA 8.1*, Comput. Phys. Commun. **178** (2008) 852, arXiv: [0710.3820 \[hep-ph\]](#) (cit. on p. 4).
- [41] NNPDF Collaboration, R. D. Ball et al., *Parton distributions with LHC data*, Nucl. Phys. B **867** (2013) 244, arXiv: [1207.1303 \[hep-ph\]](#) (cit. on p. 4).
- [42] ATLAS Collaboration, *The Pythia 8 A3 tune description of ATLAS minimum bias and inelastic measurements incorporating the Donnachie–Landshoff diffractive model*, ATL-PHYS-PUB-2016-017, 2016, URL: <https://cds.cern.ch/record/2206965> (cit. on p. 4).
- [43] E. Bothmann et al., *Event generation with Sherpa 2.2*, SciPost Phys. **7** (2019) 034, arXiv: [1905.09127 \[hep-ph\]](#) (cit. on pp. 4, 8).
- [44] D. J. Lange, *The EvtGen particle decay simulation package*, Nucl. Instrum. Meth. A **462** (2001) 152 (cit. on p. 4).
- [45] T. Sjöstrand et al., *An introduction to PYTHIA 8.2*, Comput. Phys. Commun. **191** (2015) 159, arXiv: [1410.3012 \[hep-ph\]](#) (cit. on p. 4).
- [46] ATLAS Collaboration, *ATLAS Pythia 8 tunes to 7 TeV data*, ATL-PHYS-PUB-2014-021, 2014, URL: <https://cds.cern.ch/record/1966419> (cit. on pp. 4, 14).
- [47] E. Re, *Single-top Wt-channel production matched with parton showers using the POWHEG method*, Eur. Phys. J. C **71** (2011) 1547, arXiv: [1009.2450 \[hep-ph\]](#) (cit. on p. 5).

- [48] S. Frixione, G. Ridolfi and P. Nason,
A positive-weight next-to-leading-order Monte Carlo for heavy flavour hadroproduction,
JHEP **09** (2007) 126, arXiv: [0707.3088 \[hep-ph\]](#) (cit. on p. 5).
- [49] P. Nason, *A new method for combining NLO QCD with shower Monte Carlo algorithms*,
JHEP **11** (2004) 040, arXiv: [hep-ph/0409146](#) (cit. on p. 5).
- [50] S. Frixione, P. Nason and C. Oleari,
Matching NLO QCD computations with parton shower simulations: the POWHEG method,
JHEP **11** (2007) 070, arXiv: [0709.2092 \[hep-ph\]](#) (cit. on p. 5).
- [51] S. Alioli, P. Nason, C. Oleari and E. Re, *A general framework for implementing NLO calculations in shower Monte Carlo programs: the POWHEG BOX*, **JHEP** **06** (2010) 043,
arXiv: [1002.2581 \[hep-ph\]](#) (cit. on p. 5).
- [52] NNPDF Collaboration, R. D. Ball et al., *Parton distributions for the LHC run II*,
JHEP **04** (2015) 040, arXiv: [1410.8849 \[hep-ph\]](#) (cit. on pp. 5, 8).
- [53] ATLAS Collaboration, *Studies on top-quark Monte Carlo modelling for Top2016*,
ATL-PHYS-PUB-2016-020, 2016, URL: <https://cds.cern.ch/record/2216168>
(cit. on pp. 5, 7, 14, 15).
- [54] M. Beneke, P. Falgari, S. Klein and C. Schwinn,
Hadronic top-quark pair production with NNLL threshold resummation,
Nucl. Phys. B **855** (2012) 695, arXiv: [1109.1536 \[hep-ph\]](#) (cit. on p. 5).
- [55] M. Cacciari, M. Czakon, M. Mangano, A. Mitov and P. Nason, *Top-pair production at hadron colliders with next-to-next-to-leading logarithmic soft-gluon resummation*,
Phys. Lett. B **710** (2012) 612, arXiv: [1111.5869 \[hep-ph\]](#) (cit. on pp. 5, 13).
- [56] P. Bärnreuther, M. Czakon and A. Mitov, *Percent-Level-Precision Physics at the Tevatron: Next-to-Next-to-Leading Order QCD Corrections to $q\bar{q} \rightarrow t\bar{t} + X$* ,
Phys. Rev. Lett. **109** (2012) 132001, arXiv: [1204.5201 \[hep-ph\]](#) (cit. on p. 5).
- [57] M. Czakon and A. Mitov,
NNLO corrections to top-pair production at hadron colliders: the all-fermionic scattering channels,
JHEP **12** (2012) 054, arXiv: [1207.0236 \[hep-ph\]](#) (cit. on p. 5).
- [58] M. Czakon and A. Mitov,
NNLO corrections to top pair production at hadron colliders: the quark-gluon reaction,
JHEP **01** (2013) 080, arXiv: [1210.6832 \[hep-ph\]](#) (cit. on p. 5).
- [59] M. Czakon, P. Fiedler and A. Mitov,
Total Top-Quark Pair-Production Cross Section at Hadron Colliders Through $O(\alpha_S^4)$,
Phys. Rev. Lett. **110** (2013) 252004, arXiv: [1303.6254 \[hep-ph\]](#) (cit. on p. 5).
- [60] M. Czakon and A. Mitov,
Top++: A program for the calculation of the top-pair cross-section at hadron colliders,
Comput. Phys. Commun. **185** (2014) 2930, arXiv: [1112.5675 \[hep-ph\]](#) (cit. on p. 5).
- [61] R. D. Ball et al., *The PDF4LHC21 combination of global PDF fits for the LHC Run III*,
J. Phys. G **49** (2022) 080501, arXiv: [2203.05506 \[hep-ph\]](#) (cit. on p. 5).
- [62] M. Grazzini, S. Kallweit and M. Wiesemann, *Fully differential NNLO computations with MATRIX*,
Eur. Phys. J. C **78** (2018) 537, arXiv: [1711.06631 \[hep-ph\]](#) (cit. on p. 5).

- [63] M. Aliev et al., *HATHOR – HAdronic Top and Heavy quarks crOss section calculator*, *Comput. Phys. Commun.* **182** (2011) 1034, arXiv: [1007.1327 \[hep-ph\]](#) (cit. on p. 5).
- [64] J. H. Kuhn, A. Scharf and P. Uwer,
Electroweak effects in top-quark pair production at hadron colliders, *Eur. Phys. J. C* **51** (2007) 37, arXiv: [hep-ph/0610335](#) (cit. on p. 5).
- [65] J. H. Kühn, A. Scharf and P. Uwer,
Weak Interactions in Top-Quark Pair Production at Hadron Colliders: An Update, *Phys. Rev. D* **91** (2015) 014020, arXiv: [1305.5773 \[hep-ph\]](#) (cit. on pp. 5, 13).
- [66] J. H. Kuhn, A. Scharf and P. Uwer,
Electroweak corrections to top-quark pair production in quark -antiquark annihilation, *Eur. Phys. J. C* **45** (2006) 139, arXiv: [hep-ph/0508092](#) (cit. on p. 5).
- [67] T. Ježo and P. Nason, *On the Treatment of Resonances in Next-to-Leading Order Calculations Matched to a Parton Shower*, *JHEP* **12** (2015) 065, arXiv: [1509.09071 \[hep-ph\]](#) (cit. on p. 6).
- [68] T. Ježo, J. M. Lindert and S. Pozzorini,
Resonance-aware NLOPS matching for off-shell $t\bar{t} + tW$ production with semileptonic decays, (2023), arXiv: [2307.15653 \[hep-ph\]](#), URL: <https://arxiv.org/abs/2307.15653> (cit. on p. 6).
- [69] M. Jezabek, J. H. Kuhn and T. Teubner,
Momentum distributions in $t\bar{t}$ production and decay near threshold, *Z. Phys. C* **56** (1992) 653 (cit. on p. 6).
- [70] K. Hagiwara, K. Ma and H. Yokoya,
Probing CP violation in e^+e^- production of the Higgs boson and toponia, *JHEP* **06** (2016) 048, arXiv: [1602.00684 \[hep-ph\]](#) (cit. on p. 6).
- [71] K. Hagiwara, H. Yokoya and Y.-J. Zheng,
Probing the CP properties of top Yukawa coupling at an e^+e^- collider, *JHEP* **02** (2018) 180, arXiv: [1712.09953 \[hep-ph\]](#) (cit. on p. 6).
- [72] B. Fuks, Private communication. (cit. on p. 7).
- [73] ATLAS Collaboration, *Studies of $t\bar{t}/tW$ interference effects in $b\bar{b}\ell^+\ell^-\nu\bar{\nu}$ final states with PowHEG and MADGRAPH5_AMC@NLO setups*, ATL-PHYS-PUB-2021-042, 2021, URL: <https://cds.cern.ch/record/2792254> (cit. on p. 7).
- [74] S. Frixione, E. Laenen, P. Motylinski, C. White and B. R. Webber,
Single-top hadroproduction in association with a W boson, *JHEP* **07** (2008) 029, arXiv: [0805.3067 \[hep-ph\]](#) (cit. on pp. 7, 15).
- [75] N. Kidonakis and N. Yamanaka,
Higher-order corrections for tW production at high-energy hadron colliders, *JHEP* **05** (2021) 278, arXiv: [2102.11300 \[hep-ph\]](#) (cit. on p. 7).
- [76] R. Frederix, E. Re and P. Torrielli,
Single-top t-channel hadroproduction in the four-flavour scheme with POWHEG and aMC@NLO, *JHEP* **09** (2012) 130, arXiv: [1207.5391 \[hep-ph\]](#) (cit. on p. 7).
- [77] S. Frixione, E. Laenen, P. Motylinski and B. R. Webber, *Angular correlations of lepton pairs from vector boson and top quark decays in Monte Carlo simulations*, *JHEP* **04** (2007) 081, arXiv: [hep-ph/0702198](#) (cit. on p. 7).

- [78] P. Artoisenet, R. Frederix, O. Mattelaer and R. Rietkerk, *Automatic spin-entangled decays of heavy resonances in Monte Carlo simulations*, *JHEP* **03** (2013) 015, arXiv: [1212.3460 \[hep-ph\]](#) (cit. on p. 7).
- [79] J. Campbell, T. Neumann and Z. Sullivan, *Single-top-quark production in the t-channel at NNLO*, *JHEP* **02** (2021) 040, arXiv: [2012.01574 \[hep-ph\]](#) (cit. on p. 8).
- [80] Z. L. Liu and J. Gao, *s -channel single top quark production and decay at next-to-next-to-leading-order in QCD*, *Phys. Rev. D* **98** (2018) 071501, arXiv: [1807.03835 \[hep-ph\]](#) (cit. on p. 8).
- [81] T. Gleisberg and S. Höche, *Comix, a new matrix element generator*, *JHEP* **12** (2008) 039, arXiv: [0808.3674 \[hep-ph\]](#) (cit. on p. 8).
- [82] F. Buccioni et al., *OpenLoops 2*, *Eur. Phys. J. C* **79** (2019) 866, arXiv: [1907.13071 \[hep-ph\]](#) (cit. on p. 8).
- [83] F. Cascioli, P. Maierhöfer and S. Pozzorini, *Scattering Amplitudes with Open Loops*, *Phys. Rev. Lett.* **108** (2012) 111601, arXiv: [1111.5206 \[hep-ph\]](#) (cit. on p. 8).
- [84] A. Denner, S. Dittmaier and L. Hofer, *COLLIER: A fortran-based complex one-loop library in extended regularizations*, *Comput. Phys. Commun.* **212** (2017) 220, arXiv: [1604.06792 \[hep-ph\]](#) (cit. on p. 8).
- [85] S. Schumann and F. Krauss, *A parton shower algorithm based on Catani–Seymour dipole factorisation*, *JHEP* **03** (2008) 038, arXiv: [0709.1027 \[hep-ph\]](#) (cit. on p. 8).
- [86] S. Höche, F. Krauss, M. Schönher and F. Siegert, *A critical appraisal of NLO+PS matching methods*, *JHEP* **09** (2012) 049, arXiv: [1111.1220 \[hep-ph\]](#) (cit. on p. 8).
- [87] S. Höche, F. Krauss, M. Schönher and F. Siegert, *QCD matrix elements + parton showers. The NLO case*, *JHEP* **04** (2013) 027, arXiv: [1207.5030 \[hep-ph\]](#) (cit. on p. 8).
- [88] S. Catani, F. Krauss, B. R. Webber and R. Kuhn, *QCD Matrix Elements + Parton Showers*, *JHEP* **11** (2001) 063, arXiv: [hep-ph/0109231](#) (cit. on p. 8).
- [89] S. Höche, F. Krauss, S. Schumann and F. Siegert, *QCD matrix elements and truncated showers*, *JHEP* **05** (2009) 053, arXiv: [0903.1219 \[hep-ph\]](#) (cit. on p. 8).
- [90] C. Anastasiou, L. Dixon, K. Melnikov and F. Petriello, *High-precision QCD at hadron colliders: Electroweak gauge boson rapidity distributions at next-to-next-to leading order*, *Phys. Rev. D* **69** (2004) 094008, arXiv: [hep-ph/0312266](#) (cit. on p. 8).
- [91] D. de Florian et al., *Handbook of LHC Higgs Cross Sections: 4. Deciphering the Nature of the Higgs Sector*, (2017), arXiv: [1610.07922 \[hep-ph\]](#) (cit. on p. 8).
- [92] J. Alwall et al., *The automated computation of tree-level and next-to-leading order differential cross sections, and their matching to parton shower simulations*, *JHEP* **07** (2014) 079, arXiv: [1405.0301 \[hep-ph\]](#) (cit. on p. 8).
- [93] ATLAS Collaboration, *ATLAS data quality operations and performance for 2015–2018 data-taking*, *JINST* **15** (2020) P04003, arXiv: [1911.04632 \[physics.ins-det\]](#) (cit. on p. 8).

- [94] ATLAS Collaboration, *Vertex Reconstruction Performance of the ATLAS Detector at $\sqrt{s} = 13$ TeV*, ATL-PHYS-PUB-2015-026, 2015, URL: <https://cds.cern.ch/record/2037717> (cit. on p. 9).
- [95] ATLAS Collaboration, *Muon reconstruction performance of the ATLAS detector in proton–proton collision data at $\sqrt{s} = 13$ TeV*, *Eur. Phys. J. C* **76** (2016) 292, arXiv: [1603.05598 \[hep-ex\]](https://arxiv.org/abs/1603.05598) (cit. on pp. 9, 13).
- [96] ATLAS Collaboration, *Muon reconstruction and identification efficiency in ATLAS using the full Run 2 pp collision data set at $\sqrt{s} = 13$ TeV*, *Eur. Phys. J. C* **81** (2021) 578, arXiv: [2012.00578 \[hep-ex\]](https://arxiv.org/abs/2012.00578) (cit. on pp. 9, 13).
- [97] ATLAS Collaboration, *Electron reconstruction and identification in the ATLAS experiment using the 2015 and 2016 LHC proton–proton collision data at $\sqrt{s} = 13$ TeV*, *Eur. Phys. J. C* **79** (2019) 639, arXiv: [1902.04655 \[physics.ins-det\]](https://arxiv.org/abs/1902.04655) (cit. on pp. 9, 13).
- [98] ATLAS Collaboration, *Electron and photon performance measurements with the ATLAS detector using the 2015–2017 LHC proton–proton collision data*, *JINST* **14** (2019) P12006, arXiv: [1908.00005 \[hep-ex\]](https://arxiv.org/abs/1908.00005) (cit. on pp. 9, 13).
- [99] ATLAS Collaboration, *Jet reconstruction and performance using particle flow with the ATLAS Detector*, *Eur. Phys. J. C* **77** (2017) 466, arXiv: [1703.10485 \[hep-ex\]](https://arxiv.org/abs/1703.10485) (cit. on p. 9).
- [100] ATLAS Collaboration, *Jet energy scale and resolution measured in proton–proton collisions at $\sqrt{s} = 13$ TeV with the ATLAS detector*, *Eur. Phys. J. C* **81** (2021) 689, arXiv: [2007.02645 \[hep-ex\]](https://arxiv.org/abs/2007.02645) (cit. on pp. 9, 13, 19).
- [101] M. Cacciari, G. P. Salam and G. Soyez, *The anti- k_t jet clustering algorithm*, *JHEP* **04** (2008) 063, arXiv: [0802.1189 \[hep-ph\]](https://arxiv.org/abs/0802.1189) (cit. on p. 9).
- [102] M. Cacciari, G. P. Salam and G. Soyez, *FastJet user manual*, *Eur. Phys. J. C* **72** (2012) 1896, arXiv: [1111.6097 \[hep-ph\]](https://arxiv.org/abs/1111.6097) (cit. on p. 9).
- [103] M. Cacciari and G. P. Salam, *Pileup subtraction using jet areas*, *Physics Letters B* **659** (2008) 119, ISSN: 0370-2693, URL: <http://dx.doi.org/10.1016/j.physletb.2007.09.077> (cit. on p. 9).
- [104] ATLAS Collaboration, *Performance of pile-up mitigation techniques for jets in pp collisions at $\sqrt{s} = 8$ TeV using the ATLAS detector*, *Eur. Phys. J. C* **76** (2016) 581, arXiv: [1510.03823 \[hep-ex\]](https://arxiv.org/abs/1510.03823) (cit. on pp. 9, 13).
- [105] ATLAS Collaboration, *ATLAS flavour-tagging algorithms for the LHC Run 2 pp collision dataset*, *Eur. Phys. J. C* **83** (2023) 681, arXiv: [2211.16345 \[physics.data-an\]](https://arxiv.org/abs/2211.16345) (cit. on p. 9).
- [106] ATLAS Collaboration, *ATLAS b-jet identification performance and efficiency measurement with $t\bar{t}$ events in pp collisions at $\sqrt{s} = 13$ TeV*, *Eur. Phys. J. C* **79** (2019) 970, arXiv: [1907.05120 \[hep-ex\]](https://arxiv.org/abs/1907.05120) (cit. on pp. 9, 13).
- [107] ATLAS Collaboration, *Measurement of the c-jet mistagging efficiency in $t\bar{t}$ events using pp collision data at $\sqrt{s} = 13$ TeV collected with the ATLAS detector*, *Eur. Phys. J. C* **82** (2022) 95, arXiv: [2109.10627 \[hep-ex\]](https://arxiv.org/abs/2109.10627) (cit. on pp. 9, 13).
- [108] ATLAS Collaboration, *Calibration of light-flavour b-jet mistagging rates using ATLAS proton–proton collision data at $\sqrt{s} = 13$ TeV*, ATLAS-CONF-2018-006, 2018, URL: <https://cds.cern.ch/record/2314418> (cit. on p. 9).

- [109] ATLAS Collaboration, *Performance of missing transverse momentum reconstruction with the ATLAS detector using proton–proton collisions at $\sqrt{s} = 13$ TeV*, *Eur. Phys. J. C* **78** (2018) 903, arXiv: [1802.08168 \[hep-ex\]](#) (cit. on p. 10).
- [110] Y. Afik and J. R. M. de Nova, *Quantum information with top quarks in QCD*, *Quantum* **6** (2022) 820, arXiv: [2203.05582 \[quant-ph\]](#) (cit. on p. 10).
- [111] J. A. Aguilar-Saavedra and J. A. Casas, *Improved tests of entanglement and Bell inequalities with LHC tops*, *Eur. Phys. J. C* **82** (2022) 666, arXiv: [2205.00542 \[hep-ph\]](#) (cit. on p. 10).
- [112] B. A. Betchart, R. Demina and A. Harel, *Analytic solutions for neutrino momenta in decay of top quarks*, *Nucl. Instrum. Meth. A* **736** (2014) 169, arXiv: [1305.1878 \[hep-ph\]](#) (cit. on p. 11).
- [113] ATLAS Collaboration, *Measurements of the production cross-section for a Z boson in association with b- or c-jets in proton–proton collisions at $\sqrt{s} = 13$ TeV with the ATLAS detector*, *Eur. Phys. J. C* **84** (2024) 984, arXiv: [2403.15093 \[hep-ex\]](#) (cit. on p. 12).
- [114] ATLAS Collaboration, *Dependence of the Jet Energy Scale on the Particle Content of Hadronic Jets in the ATLAS Detector Simulation*, ATL-PHYS-PUB-2022-021, 2022, URL: <https://cds.cern.ch/record/2808016> (cit. on p. 13).
- [115] ATLAS Collaboration, *Calibration of the light-flavour jet mistagging efficiency of the b-tagging algorithms with Z+jets events using 139fb^{-1} of ATLAS proton–proton collision data at $\sqrt{s} = 13$ TeV*, *Eur. Phys. J. C* **83** (2023) 728, arXiv: [2301.06319 \[hep-ex\]](#) (cit. on p. 13).
- [116] ATLAS Collaboration, *Electron and photon efficiencies in LHC Run 2 with the ATLAS experiment*, *JHEP* **05** (2024) 162, arXiv: [2308.13362 \[hep-ex\]](#) (cit. on p. 13).
- [117] ATLAS Collaboration, *Studies of the muon momentum calibration and performance of the ATLAS detector with pp collisions at $\sqrt{s} = 13$ TeV*, *Eur. Phys. J. C* **83** (2023) 686, arXiv: [2212.07338 \[hep-ex\]](#) (cit. on p. 13).
- [118] ATLAS Collaboration, *The performance of missing transverse momentum reconstruction and its significance with the ATLAS detector using 140fb^{-1} of $\sqrt{s} = 13$ TeV pp collisions*, *Eur. Phys. J. C* **85** (2025) 606, arXiv: [2402.05858 \[hep-ex\]](#) (cit. on p. 13).
- [119] ATLAS Collaboration, *E_T^{miss} performance in the ATLAS detector using 2015–2016 LHC pp collisions*, ATLAS-CONF-2018-023, 2018, URL: <https://cds.cern.ch/record/2625233> (cit. on p. 13).
- [120] ATLAS Collaboration, *A detailed map of Higgs boson interactions by the ATLAS experiment ten years after the discovery*, *Nature* **607** (2022) 52, arXiv: [2207.00092 \[hep-ex\]](#) (cit. on p. 13), Erratum: *Nature* **612** (2022) E24.
- [121] J. Butterworth et al., *PDF4LHC recommendations for LHC Run II*, *J. Phys. G* **43** (2016) 023001, arXiv: [1510.03865 \[hep-ph\]](#) (cit. on p. 14).
- [122] M. Bähr et al., *Herwig++ physics and manual*, *Eur. Phys. J. C* **58** (2008) 639, arXiv: [0803.0883 \[hep-ph\]](#) (cit. on p. 14).
- [123] J. Bellm et al., *Herwig 7.0/Herwig++ 3.0 release note*, *Eur. Phys. J. C* **76** (2016) 196, arXiv: [1512.01178 \[hep-ph\]](#) (cit. on p. 14).

- [124] L. A. Harland-Lang, A. D. Martin, P. Motylinski and R. S. Thorne, *Parton distributions in the LHC era: MMHT 2014 PDFs*, *Eur. Phys. J. C* **75** (2015) 204, arXiv: [1412.3989 \[hep-ph\]](#) (cit. on p. 14).
- [125] ATLAS Collaboration, *Studies on the improvement of the matching uncertainty definition in top-quark processes simulated with PowHEG+PYTHIA8*, ATL-PHYS-PUB-2023-029, 2013, URL: <https://cds.cern.ch/record/2872787> (cit. on p. 14).
- [126] H. Brooks and P. Skands, *Coherent showers in decays of colored resonances*, *Phys. Rev. D* **100** (2019) 076006, arXiv: [1907.08980 \[hep-ph\]](#) (cit. on p. 14).
- [127] C. Bierlich et al., *A comprehensive guide to the physics and usage of PYTHIA 8.3*, *SciPost Phys. Codeb.* **2022** (2022) 8, arXiv: [2203.11601 \[hep-ph\]](#) (cit. on p. 14).
- [128] ATLAS Collaboration, *Measurements of observables sensitive to colour reconnection in $t\bar{t}$ events with the ATLAS detector at $\sqrt{s} = 13$ TeV*, *Eur. Phys. J. C* **83** (2023) 518, arXiv: [2209.07874 \[hep-ex\]](#) (cit. on p. 14).
- [129] ATLAS Collaboration, *A study of different colour reconnection settings for Pythia8 generator using underlying event observables*, ATL-PHYS-PUB-2017-008, 2017, URL: <https://cds.cern.ch/record/2262253> (cit. on p. 14).
- [130] N. Kidonakis, *Two-loop soft anomalous dimensions for single top quark associated production with a W^- or H^-* , *Phys. Rev. D* **82** (2010) 054018, arXiv: [1005.4451 \[hep-ph\]](#) (cit. on p. 15).
- [131] J. Alwall et al., *Comparative study of various algorithms for the merging of parton showers and matrix elements in hadronic collisions*, *Eur. Phys. J. C* **53** (2008) 473, arXiv: [0706.2569 \[hep-ph\]](#) (cit. on p. 15).
- [132] ATLAS Collaboration, *Search for the standard model Higgs boson produced in association with top quarks and decaying into a $b\bar{b}$ pair in pp collisions at $\sqrt{s} = 13$ TeV with the ATLAS detector*, *Phys. Rev. D* **97** (2018) 072016, arXiv: [1712.08895 \[hep-ex\]](#) (cit. on p. 15).
- [133] G. Cowan, K. Cranmer, E. Gross and O. Vitells, *Asymptotic formulae for likelihood-based tests of new physics*, *Eur. Phys. J. C* **71** (2011) 1554, arXiv: [1007.1727 \[physics.data-an\]](#) (cit. on p. 16), Erratum: *Eur. Phys. J. C* **73** (2013) 2501.
- [134] R. D. Cousins, *Lectures on Statistics in Theory: Prelude to Statistics in Practice*, (2018), arXiv: [1807.05996 \[physics.data-an\]](#) (cit. on p. 17).
- [135] A. Pinto et al., *Uncertainty components in profile likelihood fits*, *Eur. Phys. J. C* **84** (2024) 593, arXiv: [2307.04007 \[physics.data-an\]](#) (cit. on pp. 20, 27, 31).